The Astrophysical Journal, 897:130 (19pp), 2020 July 10 https://doi.org/10.3847/1538-4357/ab9ac6

Common Envelope Wind Tunnel: The Effects of Binary Mass Ratio and Implications for the Accretion-driven Growth of LIGO Binary Black Holes

Soumi De[1,2], Morgan MacLeod[3], Rosa Wallace Everson[4,5,10], Andrea Antoni[6], Ilya Mandel[5,7,8,9], and Enrico Ramirez-Ruiz[4,5]

[1] Department of Physics, Syracuse University, Syracuse, NY 13244, USA; sde101@syr.edu
[2] Kavli Institute for Theoretical Physics, University of California, Santa Barbara, CA 93106, USA
[3] Harvard-Smithsonian Center for Astrophysics, 60 Garden Street, Cambridge, MA 02138, USA
[4] Department of Astronomy and Astrophysics, University of California, Santa Cruz, CA 95064, USA
[5] Niels Bohr Institute, University of Copenhagen, Blegdamsvej 17, DK-2100 Copenhagen, Denmark
[6] Department of Astronomy, University of California, Berkeley, CA 94720, USA
[7] School of Physics and Astronomy, Monash University, Clayton, VIC 3800, Australia
[8] OzGrav: The ARC Centre of Excellence for Gravitational Wave Discovery, Australia
[9] School of Physics and Astronomy, University of Birmingham, Edgbaston, Birmingham B15 2TT, UK
Received 2019 October 29; revised 2020 May 18; accepted 2020 May 21; published 2020 July 10

Abstract

We present three-dimensional local hydrodynamic simulations of flows around objects embedded within stellar envelopes using a "wind tunnel" formalism. Our simulations model the common envelope dynamical inspiral phase in binary star systems in terms of dimensionless flow characteristics. We present suites of simulations that study the effects of varying the binary mass ratio, stellar structure, equation of state, relative Mach number of the object's motion through the gas, and density gradients across the gravitational focusing scale. For each model, we measure coefficients of accretion and drag experienced by the embedded object. These coefficients regulate the coupled evolution of the object's masses and orbital tightening during the dynamical inspiral phase of the common envelope. We extrapolate our simulation results to accreting black holes with masses comparable to that of the population of LIGO black holes. We demonstrate that the mass and spin accrued by these black holes per unit orbital tightening are directly related to the ratio of accretion to drag coefficients. We thus infer that the mass and dimensionless spin of initially nonrotating black holes change by of order 1% and 0.05, respectively, in a typical example scenario. Our prediction that the masses and spins of black holes remain largely unmodified by a common envelope phase aids in the interpretation of the properties of the growing observed population of merging binary black holes. Even if these black holes passed through a common envelope phase during their assembly, features of mass and spin imparted by previous evolutionary epochs should be preserved.

Unified Astronomy Thesaurus concepts: Accretion (14); Hydrodynamics (1963); Hydrodynamical simulations (767); Close binary stars (254); Common envelope binary stars (2156)

Supporting material: animation, interactive figures

1. Introduction

A common envelope phase is a short episode in the life of a binary star system in which the two components of the binary evolve inside a shared envelope. Common envelope phases typically occur when one of the stars in the binary expands, engulfing its companion object (Paczynski 1976; Taam et al. 1978; Iben & Livio 1993; Taam & Ricker 2010; Ivanova et al. 2013; de Marco & Izzard 2017). Inside the common envelope, the embedded companion object interacts with the material flowing past it, giving rise to dynamical friction drag forces (Chandrasekhar 1943; Ostriker 1999). These drag forces lead to an orbital tightening as the two objects spiral in. Common envelope phases are thought to be critical to the formation of compact-object binaries that subsequently merge through the emission of gravitational radiation (Smarr & Blandford 1976; van den Heuvel 1976; see, e.g., Mandel & Farmer 2018, for a review). Thus, understanding the common envelope phase is important for understanding the formation channel and evolutionary history of merging compact-object binaries, such as those observed by the LIGO and Virgo gravitational-wave detectors (Aasi et al. 2015; Acernese et al. 2015).

Significant theoretical effort has gone into modeling the physical processes of common envelope phases. This work has been challenging because of the range of physically significant spatial and temporal scales, as well as the range of potentially important physical processes (Iben & Livio 1993; Ivanova et al. 2013). One crucial example is the energy release from the recombination of ionized hydrogen and helium (Lucy 1967; Roxburgh 1967; Han et al. 1994, 2002; Nandez et al. 2015; Ivanova & Nandez 2016). Efforts have often focused on either global hydrodynamic modeling of the overall encounter (for example, the recent work of Ricker & Taam 2007; Passy et al. 2012; Ricker & Taam 2012; Ohlmann et al. 2016a, 2016b; Iaconi et al. 2017, 2018; Chamandy et al. 2018, 2019a, 2019b; Fragos et al. 2019; Reichardt et al. 2019) or local hydrodynamic simulations that simplify and zoom in on one aspect of the larger encounter (e.g., Fryxell et al. 1987; Fryxell & Taam 1989; Taam & Fryxell 1989; Sandquist et al. 1998; MacLeod & Ramirez-Ruiz 2015a, 2015b; MacLeod et al. 2017).

Global simulations attempt to model the full spatial extent of binary systems for many orbital timescales. This approach captures the full extent of the envelope structure and the physical complexities involved. However, this also leads to the simulations being highly computationally expensive, limiting the choice to

[10] NSF Graduate Research Fellow.

exploring a small parameter space with high resolution, or exploring a large parameter space with low resolution. Local simulations, on the other hand, attempt to isolate and study flow morphologies around the embedded object with a broad parameter space and high resolution. This approach does not capture the full geometry in a single simulation. However, the goal is to model flow conditions representative of different regions or times within the overall event. Adding together results from multiple such simulations can help to interpret the outcomes of global models and physics of the full common envelope interaction. A synthesis of the global and local simulations offers a pathway toward understanding the complex gas dynamics of common envelope phases.

This paper extends previous work on local simulations of gas flow past an object inspiraling through the gaseous surroundings of a common envelope. We use the "wind tunnel" formalism, first presented in MacLeod & Ramirez-Ruiz (2015b) and expanded in MacLeod et al. (2017), to study the flow past a compact object embedded in the stellar envelope of a red giant or asymptotic giant branch star. The stellar profile of the donor at the onset of the dynamically unstable mass transfer depends on the mass ratio and initial separation between the centers of the two stars in the binary. We focus in particular on the variation in the properties as the binary mass ratio changes, and we present two suites of simulations with ideal gas equations of state characterized by adiabatic exponents $\gamma = 4/3$ and $\gamma = 5/3$, which bracket the range of typical values in stellar envelopes (e.g., MacLeod et al. 2017; Murguia-Berthier et al. 2017).

This paper is organized as follows. In Section 2 we describe the common envelope flow parameters and conditions. We describe gravitational focusing in common envelope flows and illustrate the parameter space that controls the properties of the local flow past an object embedded in a common envelope. In Section 3 we describe the wind tunnel setup for hydrodynamic simulations, describe the model parameters, illustrate how the flow evolves through the simulations, and provide the quantities that we compute as a product of the simulations. We present hydrodynamic simulations using the wind tunnel setup for common envelope flows with a $\gamma = 4/3$ and $\gamma = 5/3$ equation of state, describe the flow characteristics, and provide the results obtained from the simulations. In Section 4, we extrapolate our simulation results for the scenario of a black hole inspiraling through the envelope of its companion. We estimate the mass and spin accrued by black holes during the common envelope phase and derive implications for the effect of this phase on the properties of black holes in merging binaries that constitute LIGO-Virgo sources. We conclude in Section 5. A companion paper, Everson et al. (2020), explores the validity of the expression of realistic stellar models in the dimensionless terms adopted here.

2. Common Envelope Flow Parameters and Conditions

2.1. Characteristic Scales

The Hoyle–Lyttleton (HL) theory of accretion (Hoyle & Lyttleton 1939; Bondi & Hoyle 1944; Edgar 2004) is used extensively to describe accretion onto a compact object having a velocity relative to the ambient medium. We use that as a starting point to consider an embedded, accreting object of mass M_2 moving with velocity v_∞ relative to a surrounding gas of unperturbed density ρ_∞ that follows a stellar profile typical of a common envelope. The characteristic impact parameter inside which gas is gravitationally focused toward the embedded object and can potentially accrete is set by the Bondi–Hoyle accretion radius, written as

$$R_{\rm a,BH} = \frac{2GM_2}{v_\infty^2 + c_{s,\infty}^2}. \quad (1)$$

For an object in significantly supersonic motion $v_\infty > c_{s,\infty}$, where $c_{s,\infty}$ is the sound speed of the gas, the Bondi–Hoyle accretion radius can be replaced by the HL accretion radius, written as

$$R_{\rm a,HL} = \frac{2GM_2}{v_\infty^2}. \quad (2)$$

During the dynamical inspiral phase of common envelope evolution for a system consisting of a black hole in a red supergiant, the embedded object moves supersonically through the host envelope (e.g., MacLeod & Ramirez-Ruiz 2015a). This scenario can be appropriately described by HL scales (with accretion radius $R_{\rm a,HL}$), and this is the regime that we model in this work. We refer to $R_{\rm a,HL}$ as $R_{\rm a}$ henceforth.

HL accretion implies a characteristic interaction cross section of $\pi R_{\rm a}^2$ (Hoyle & Lyttleton 1939). The corresponding mass flux through this cross section and potential mass accretion rate in HL flows can be written as (Edgar 2004)

$$\dot{M}_{\rm HL} = \pi R_{\rm a}^2 \rho_\infty v_\infty. \quad (3)$$

The characteristic scales for momentum and energy dissipation due to gravitational interaction (Ostriker 1999) can be derived from this cross section as well. The characteristic scale for the momentum dissipation rate, or force, is

$$F_{\rm HL} = \pi R_{\rm a}^2 \rho_\infty v_\infty^2 = \dot{M}_{\rm HL} v_\infty, \quad (4)$$

and the characteristic energy dissipation rate is

$$\dot{E}_{\rm HL} = \pi R_{\rm a}^2 \rho_\infty v_\infty^3 = \dot{M}_{\rm HL} v_\infty^2, \quad (5)$$

if we assume that all momentum and energy passing through the interaction cross section $\pi R_{\rm a}^2$ are dissipated.

2.2. Common Envelope Parameters

We imagine that the embedded object M_2 is spiraling in to tighter orbital separations within the envelope of a giant-star primary. The core of the primary is fixed at $r = 0$, and the orbital radius of M_2 within the primary's envelope is $r = a$. Thus, the stellar cores are separated by a distance a, smaller than the original radius of the primary. We use $M_1(r)$ to denote the mass of the primary that is enclosed by the orbit of M_2. Therefore, the Keplerian orbital velocity is $v_{\rm k} = \sqrt{GM/a}$, where $M = M_1(a) + M_2$ is the total enclosed mass of the binary (mass outside of the orbital separation a does not contribute to the orbital velocity). The relative velocity of the secondary to the envelope gas, v_∞, is related to the Keplerian velocity of the secondary as $v_\infty = f_{\rm k} v_k$. Thus, $f_{\rm k}$ is the fraction of the Keplerian velocity that contributes to the relative velocity. In our simulations, we adopt the simplification $f_{\rm k} = 1$. However, $f_{\rm k} < 1.0$ is possible if the orbital motion of the embedded object is partially synchronized to the donor's envelope.

Given a relative velocity set by the orbital motion, the ratio of the gravitational focusing scale, $R_{\rm a}$, to the orbital separation,

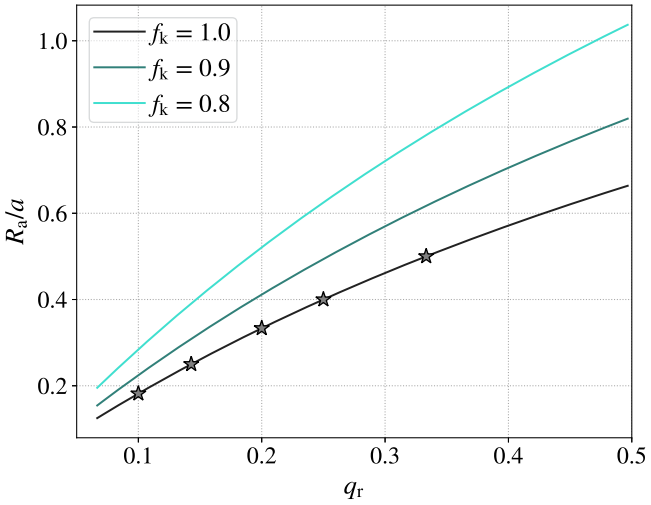

Figure 1. Fraction of the orbital separation falling within the gravitational focusing radius of the embedded object, R_a/a, as a function of the binary mass ratio q_r. The plot shows the relation for $f_k = 1.0$, 0.9, and 0.8, where f_k is the fraction of the Keplerian velocity contributing to the relative velocity. Markers show the points for which hydrodynamical simulations have been performed in this paper. For small mass ratios, the accretion radius of M_2 is small relative to the orbital separation. When q_r is large, R_a sweeps out a significant fraction of the orbital separation. For fixed M_2, q_r increases as the embedded object spirals further into the envelope of the primary.

a, is (MacLeod et al. 2017)

$$\frac{R_a}{a} = \frac{2}{f_k^2}\frac{M_2}{M} = \frac{2}{f_k^2}\frac{1}{1+q_r^{-1}}, \tag{6}$$

where $q_r = M_2/M_1(r)$ is the mass ratio between the embedded object and the mass enclosed by its orbit. Therefore, for a given value of q_r, one can calculate R_a in terms of a. The variation of R_a in terms of a with q_r is shown in Figure 1 for $f_k = 1$, 0.9, and 0.8. As q_r increases, R_a/a also increases and gives an approximate scale for the fraction of the envelope affected by the embedded object.

The HL formalism assumes a homogeneous background for the embedded object. In practice, such a situation does not arise in common envelope encounters. As demonstrated in Figure 1, R_a/a can be a large fraction of unity for typical mass ratios. Therefore, the gaseous medium with which the embedded object interacts spans a range of densities and temperatures (MacLeod & Ramirez-Ruiz 2015a).

The flow upstream Mach number is the ratio of orbital velocity to sound speed,

$$\mathcal{M}_\infty = \frac{v_\infty}{c_{s,\infty}}, \tag{7}$$

where we specify $c_{s,\infty}$ to be the sound speed measured at radius $r = a$ within the common envelope gas. Furthermore, the density gradient in stellar profiles can be expressed in terms of a local density scale height at the location of the embedded object as

$$H_\rho = -\rho\frac{dr}{d\rho}. \tag{8}$$

The number of scale heights encompassed by the accretion radius is then quantified by the ratio

$$\epsilon_\rho = \frac{R_a}{H_\rho}, \tag{9}$$

which is, like other quantities, evaluated at the location of the embedded object. This density gradient breaks the symmetry of the flow envisioned in the HL scenario and gives the flow a net angular momentum relative to the accreting object (MacLeod & Ramirez-Ruiz 2015a, 2015b; MacLeod et al. 2017; Murguia-Berthier et al. 2017).

MacLeod et al. (2017) showed that there is a clear relation between Mach number and density gradient for typical common envelope flows when the (local) envelope structure is approximated as a polytrope with index

$$\Gamma_s = \left(\frac{d\ln P}{d\ln\rho}\right)_{\rm envelope}. \tag{10}$$

Under the simplification of an ideal gas equation of state with adiabatic index γ, we can rewrite the hydrostatic equilibrium condition of the envelope as a relationship between $\mathcal{M}_\infty$ and ϵ_ρ (Equation (18) of MacLeod et al. 2017),

$$\mathcal{M}_\infty^2 = \epsilon_\rho\frac{(1+q_r)^2}{2q_r}f_k^4\left(\frac{\Gamma_s}{\gamma}\right). \tag{11}$$

This relation reduces the parameter space to a set of specific combinations of ϵ_ρ, $\mathcal{M}_\infty$, and q_r values that are realized in common envelope phases. The validity of this approximation in the context of detailed stellar evolution models is discussed in Everson et al. (2020), who argue that the simulations presented in this paper are still applicable to a wide range of detailed stellar models described by a realistic equation of state.

3. Hydrodynamic Simulations

In this section we describe hydrodynamic simulations in the common envelope wind tunnel formalism (MacLeod et al. 2017) that explore the effects of varying the binary mass ratio on coefficients of drag and accretion realized during the dynamical inspiral of an object through the envelope of its companion.

3.1. Numerical Method

The common envelope wind tunnel model used in this work is a hydrodynamic setup using the FLASH adaptive mesh refinement hydrodynamics code (Fryxell et al. 2000). A full description of the model is given in Section 3 of MacLeod et al. (2017). The basic premise is that the complex geometry of a full common envelope scenario is replaced with a 3D Cartesian wind tunnel surrounding a hypothetical embedded object. Flow moves past the embedded object, and we are able to measure rates of mass accretion and drag forces.

In the common envelope wind tunnel, flows are injected from the $-x$ boundary of the computational domain past a gravitating point mass, located at the coordinate origin of the three-dimensional domain. To simulate accretion, the point mass is surrounded by a low-pressure "sink" of radius R_s. The gas obeys an ideal gas equation of state $P = (\gamma - 1)\rho e$, where e is the specific internal energy. The profile of inflowing material is defined by its upstream Mach number, $\mathcal{M}_\infty$, and the ratio of the accretion radius to the density scale height, ϵ_ρ. Calculations are performed in code units $R_a = v_\infty = \rho_\infty = 1$. Here ρ_∞ is the density of the unperturbed profile at the location of the embedded object. This gives a time unit of $R_a/v_\infty = 1$, which is the time taken by the flow to cross the accretion

radius. The binary separation a in code units is

$$\frac{a}{R_a} = \frac{1}{2} f_k^2 (1 + q_r^{-1}). \quad (12)$$

The density profile of the gas in the $\hat{y}$-direction is that of a polytrope with index Γ_s in hydrostatic equilibrium with a gravitational force

$$\vec{a}_{\mathrm{grav},1} = -\frac{GM_1(r)}{(y - y_1)^2}\hat{y}, \quad (13)$$

which represents the gravitational force from the primary star's enclosed mass, $M_1(r)$. The density scale height, sound speed, and upstream Mach number vary across this profile as they would in a polytropic star. At the $+y$ and $\pm z$ boundaries, a "diode" boundary condition is applied, which allows material to leave but not enter into the domain.

The size of the domain is set by the mass ratio of the binary system and the effective size of the binary orbit, as described by Equation (12). Gravitationally focused gas flows are sensitive to the distance over which they converge and the size of the wake that they leave (e.g., Ostriker 1999). In varying the binary mass ratio, it is important to capture this physical property of differing ratio of the gravitational focus radius to the physical size of the system, Equation (12). In order to capture the full flow, our domain has a diameter equal to the binary separation a, implying that it extends a distance $\pm a/2 = (1 + q_r^{-1})R_a/4$ about the origin in the $\pm x$, $\pm y$, and $\pm z$ directions.

This domain is spatially resolved by cubic blocks that have extent of $R_a/2$ in each direction, and each block is made of 8^3 zones. The largest zones have length $R_a/16$. We allow for five levels of adaptive mesh refinement, giving the smallest zones length $R_a/256$. We enforce maximum refinement around the embedded object at all times.

3.2. Model Parameters

The simulations that we present later in this section assume $\Gamma_s = \gamma$ and $f_k = 1$. We are therefore modeling constant entropy stellar envelope material (as in a convective envelope of a giant star) and relative velocities between the embedded object and the background gas equal to the Keplerian velocity. All models adopt a sink radius for measuring accretion of $R_s = 0.05R_a$ around the embedded object. In Section 4.1, we perform simulations with varying sink radius and discuss the dependence of our results on this parameter.

This leaves three flow parameters in Equation (11): $\mathcal{M}_\infty$, ϵ_ρ, and q_r, only two of which can be chosen independently. Figure 2 shows the simulation grid presented in this paper and those in MacLeod & Ramirez-Ruiz (2015b) and MacLeod et al. (2017) in the $\mathcal{M}_\infty - \epsilon_\rho$ space. The simulations in this paper expand the parameter space covered in the previous papers with a broader range of $\mathcal{M}_\infty$ (therefore ϵ_ρ) and, crucially, models of varying mass ratio, q_r. We construct a grid of $q_r - \mathcal{M}_\infty$ values, with q_r values 1/10, 1/7, 1/5, 1/4, and 1/3. For each value of q_r we perform simulations with $\mathcal{M}_\infty$ of 1.15, 1.39, 1.69, 2.2, 2.84, 3.48, and 5.0. It was shown in MacLeod & Ramirez-Ruiz (2015a) with the help of MESA simulations of 1–16$M_\odot$ stars evolved from the zero-age main sequence to the giant branch expansion that typical upstream Mach number values range from $\mathcal{M}_\infty \approx 2$ in the deep interior to $\mathcal{M}_\infty \gtrsim 5$ near the stellar limb. Extending these results in Everson et al. (2020), MESA is used to evolve a broader range of stellar masses 3–90$M_\odot$ with binary mass ratios of 0.1–0.35, finding $1.5 \lesssim \mathcal{M}_\infty < 7$ in giant branch stellar envelopes. It should be noted that the Mach number values discussed here and used as model parameters are defined upstream of the flow. Mach number values would differ when measured in the vicinity of the object, as material might then have crossed a shock and been compressed or heated, such as those measured in Iaconi et al. (2018).

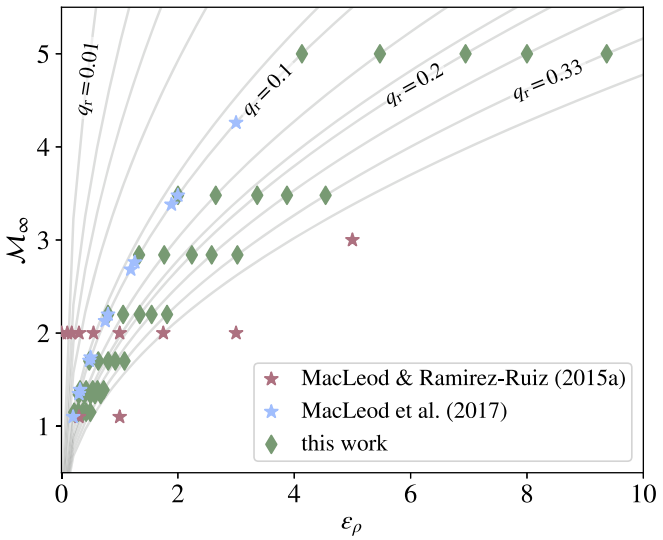

Figure 2. Points in the $\mathcal{M}_\infty$–ϵ_ρ space representing flow parameters for simulations performed with the "wind tunnel" setup. For polytropic envelopes, each combination of $\mathcal{M}_\infty$ and ϵ_ρ has a corresponding q_r value (MacLeod et al. 2017). Simulations are shown on lines of constant q_r, with the exception of three simulations from MacLeod & Ramirez-Ruiz (2015a) that do not follow the polytropic relation. The simulations in this work expand on the previous work as labeled, extending across both axes to higher Mach numbers and steeper density gradients, significantly extending coverage across the region of parameter space realized in realistic stellar profiles as detailed in Everson et al. (2020).

Tabulated model parameters are presented in Tables 1 and 2. We divide our discussion in the subsequent sections to consider the $\gamma = \Gamma_s = 4/3$ and $\gamma = \Gamma_s = 5/3$ models separately.

3.3. Model Time Evolution and Diagnostics

In Figure 3 (animated version online) we show the time evolution of a representative model (A3) with parameters $\gamma = 4/3$, $q_r = 1/10$, and $\mathcal{M}_\infty = 1.69$. The top panel in Figure 3 shows a slice through the orbital ($z = 0$) plane of the binary, with the white circle at the origin representing the absorbing sink around the embedded companion object. We show a section of the computational domain extending between $\pm R_a$. The full domain extends between $\pm(1 + q_r^{-1})R_a/4 = \pm 2.75R_a$ in each direction. The background gas injected into the domain at the $-x$ boundary, with speed $\mathcal{M}_\infty$, carries with it the density profile set by ϵ_ρ (the center of the primary is located at $y = -a$, so the density increases with decreasing y). Once material enters the domain, it is gravitationally focused by the embedded object and a bow shock forms owing to the supersonic motion of the embedded object relative to the gas. Denser material is drawn in from deeper within the star $y < 0$, such that asymmetry is introduced into the bow shock, and net rotation is imparted into the post-shock flow (MacLeod & Ramirez-Ruiz 2015a; MacLeod et al. 2017). While most of the injected material exits the domain through the $+x$ and $+y$ boundaries, some is accreted into the central sink.

Table 1
Input Parameters (q_r, $\mathcal{M}_\infty$, ϵ_ρ) and Results (C_a, C_d) for $\gamma = 4/3$ Simulations

Name	γ	q_r	$\mathcal{M}_\infty$	ϵ_ρ	C_a	C_d
A1	4/3	0.1	1.15	0.22	0.70	1.20
A2	4/3	0.1	1.39	0.32	0.77	1.44
A3	4/3	0.1	1.69	0.47	0.66	1.60
A4	4/3	0.1	2.20	0.80	0.38	1.91
A5	4/3	0.1	2.84	1.33	0.10	3.36
A6	4/3	0.1	3.48	2.00	0.07	5.44
A7	4/3	0.1	5.00	4.13	0.04	18.92
A8	4/3	0.143	1.15	0.29	0.74	1.03
A9	4/3	0.143	1.39	0.42	0.65	1.20
A10	4/3	0.143	1.70	0.63	0.52	1.22
A11	4/3	0.143	2.20	1.06	0.26	1.41
A12	4/3	0.143	2.84	1.77	0.09	2.93
A13	4/3	0.143	3.48	2.65	0.10	5.15
A14	4/3	0.143	5.00	5.47	0.07	19.38
A15	4/3	0.2	1.15	0.37	0.80	0.80
A16	4/3	0.2	1.39	0.54	0.76	1.01
A17	4/3	0.2	1.70	0.80	0.45	0.97
A18	4/3	0.2	2.20	1.34	0.22	1.05
A19	4/3	0.2	2.84	2.24	0.11	2.02
A20	4/3	0.2	3.48	3.36	0.09	4.34
A21	4/3	0.2	5.00	6.94	0.29	12.93
A22	4/3	0.25	1.15	0.42	0.79	0.65
A23	4/3	0.25	1.39	0.62	0.74	0.83
A24	4/3	0.25	1.70	0.93	0.38	0.82
A25	4/3	0.25	2.20	1.55	0.23	0.85
A26	4/3	0.25	2.84	2.58	0.13	1.66
A27	4/3	0.25	3.48	3.87	0.13	3.11
A28	4/3	0.25	5.00	8.00	0.61	7.73
A29	4/3	0.3333	1.15	0.50	0.64	0.53
A30	4/3	0.3333	1.39	0.73	0.62	0.65
A31	4/3	0.3333	1.70	1.08	0.37	0.61
A32	4/3	0.3333	2.20	1.81	0.23	0.65
A33	4/3	0.3333	2.84	3.02	0.13	1.25
A34	4/3	0.3333	3.48	4.54	0.18	1.91
A35	4/3	0.3333	5.00	9.37	1.06	5.28

Note. The C_a, C_d entries are median values computed over simulation times $10R_a/v_\infty < t < 30R_a/v_\infty$.

Table 2
Input Parameters (q_r, $\mathcal{M}_\infty$, ϵ_ρ) and Results (C_a, C_d) for $\gamma = 5/3$ Simulations

Name	γ	q_r	$\mathcal{M}_\infty$	ϵ_ρ	C_a	C_d
B1	5/3	0.1	1.15	0.22	0.36	0.79
B2	5/3	0.1	1.39	0.32	0.38	0.95
B3	5/3	0.1	1.69	0.47	0.21	0.99
B4	5/3	0.1	2.20	0.80	0.14	1.35
B5	5/3	0.1	2.84	1.33	0.05	2.07
B6	5/3	0.1	3.48	2.00	0.02	3.03
B7	5/3	0.1	5.00	4.13	0.01	6.22
B8	5/3	0.143	1.15	0.29	0.36	0.58
B9	5/3	0.143	1.39	0.42	0.35	0.79
B10	5/3	0.143	1.70	0.63	0.24	0.85
B11	5/3	0.143	2.20	1.06	0.13	1.14
B12	5/3	0.143	2.84	1.77	0.05	1.63
B13	5/3	0.143	3.48	2.65	0.03	2.42
B14	5/3	0.143	5.00	5.47	0.03	5.70
B15	5/3	0.2	1.15	0.37	0.38	0.40
B16	5/3	0.2	1.39	0.54	0.37	0.57
B17	5/3	0.2	1.70	0.80	0.22	0.65
B18	5/3	0.2	2.20	1.34	0.13	0.84
B19	5/3	0.2	2.84	2.24	0.06	1.24
B20	5/3	0.2	3.48	3.36	0.06	1.85
B21	5/3	0.2	5.00	6.94	0.04	4.76
B22	5/3	0.25	1.15	0.42	0.39	0.32
B23	5/3	0.25	1.39	0.62	0.39	0.46
B24	5/3	0.25	1.70	0.93	0.20	0.54
B25	5/3	0.25	2.20	1.55	0.09	0.65
B26	5/3	0.25	2.84	2.58	0.07	1.03
B27	5/3	0.25	3.48	3.87	0.07	1.54
B28	5/3	0.25	5.00	8.00	0.11	3.55
B29	5/3	0.3333	1.15	0.50	0.42	0.17
B30	5/3	0.3333	1.39	0.73	0.35	0.31
B31	5/3	0.3333	1.70	1.08	0.21	0.42
B32	5/3	0.3333	2.20	1.81	0.10	0.50
B33	5/3	0.3333	2.84	3.02	0.08	0.80
B34	5/3	0.3333	3.48	4.54	0.09	1.24
B35	5/3	0.3333	5.00	9.37	0.15	2.76

Note. The C_a, C_d entries are median values computed over simulation times $10\,R_a/v_\infty < t < 30\,R_a/v_\infty$.

As the simulation progresses, we monitor rates of mass and momentum accretion into the central sink (Equations (24) and 25 of MacLeod et al. 2017), as well as the gaseous dynamical friction drag force that arises from the overdensity in the wake of the embedded object (Equation (28) of MacLeod et al. 2017). We define the coefficients of accretion and drag to be the multiple of their corresponding HL values, Equations (3) and (4), respectively, realized in our simulations. That is, the coefficient of accretion is

$$C_a = \frac{\dot{M}}{\pi R_a^2 \rho_\infty v_\infty} = \frac{\dot{M}}{M_{HL}}, \tag{14}$$

where $\dot{M}$ is the mass accretion rate measured in the simulation. The coefficient of drag is

$$C_d = \frac{F_{df} + F_{\dot{p}_x}}{\pi R_a^2 \rho_\infty v_\infty^2} = \frac{F_d}{F_{HL}}, \tag{15}$$

where F_{df} is the dynamical friction drag force, $F_{\dot{p}_x}$ is the force due to linear momentum accretion, and $F_d = F_{df} + F_{\dot{p}_x}$ is the net drag force acting on the embedded object due to the gas. F_{df} is computed by performing a volume integral over the spherical shell of inner radius R_s and outer radius $(1 + q_r^{-1})R_a/4$ (the size of the computational domain in the $\pm x$, $\pm y$, $\pm z$ directions). The bottom panel of Figure 3 shows C_a and C_d as a function of time for model A3. We run our simulations for a duration $t = 30R_a/v_\infty$ (i.e., 30× code units). The flow sets up during an initial transient phase, which is $\approx 8R_a/v_\infty$ for model A3 presented in Figure 3, after which the rates of accretion and drag subside to relatively stable values. The upstream density gradient imparts turbulence to the flow, which introduces a chaotic time variability to the accretion rate and drag. Therefore, we report median values of the C_a and C_d time series from the steady-state duration of the flow, $10\,R_a/v_\infty < t < 30\,R_a/v_\infty$ in the remainder of the paper, though C_a and C_d are typically close to their steady-state values after a time a/v_∞.

Recently, Chamandy et al. (2019a) have undertaken a detailed analysis of forces in their global models of common envelope phases. One of their findings is that during the dynamical inspiral phase, flow properties and forces are very similar to those realized in local simulations such as those

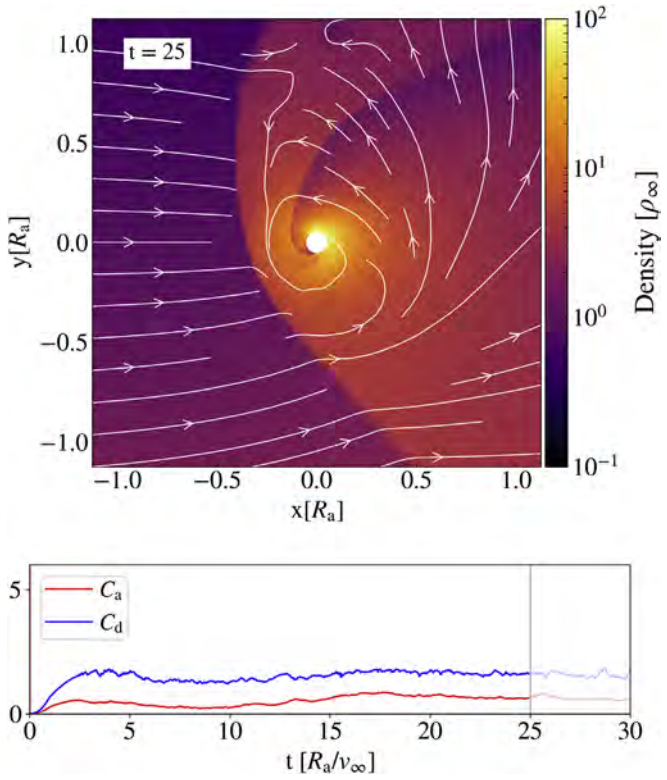

Figure 3. Movie of a simulation showing flow of material in the vicinity of an object, embedded in the envelope of its companion star during a common envelope interaction. The simulation has been performed with ideal gas equation of state adiabatic constant $\gamma = 4/3$, mass ratio $q_r = 0.1$, and upstream Mach number $\mathcal{M}_\infty = 1.69$ in the "wind tunnel" setup. The top panel shows the density in units of ρ_∞ in the orbital (x–y) plane of the binary, with the white circle at the coordinate origin representing the embedded companion object. The lines with arrowheads in white represent streamlines following the velocity field in the flow. Material enters into the domain from the $-x$ direction, and the coefficient of accretion C_a and the coefficient of drag C_d values are measured in response to the incoming conditions. Supersonic flow of material past the object results in a large pressure difference, causing formation of a shock wave. The bottom panel shows the time series of coefficients of accretion C_a (in red) and drag C_d (blue) for the full simulation. The gray vertical line tracks the instantaneous C_a, C_d values as the simulation progresses. The time quoted in the movie is in code units R_a/v_∞, where R_a is the accretion radius and v_∞ is the relative velocity of the flow past the embedded object.

(An animation of this figure is available.)

presented here. For example, Figure 3 is very similar to Figure 7 of Chamandy et al. (2019a).

3.4. Gas Flow

In this section, we discuss the properties and morphology of gas flow in our common envelope wind tunnel experiments for the models tabulated in Tables 1 and 2. We focus, in particular, on the differences that arise as we vary the dimensionless characteristics of the flow in the form of upstream Mach number, mass ratio, and gas adiabatic index.

3.4.1. Dependence on Mach Number, $\mathcal{M}_\infty$

Figures 4 and 5 show slices of density and Mach number through the orbital (x–y) plane from the models with $q_r = 1/10$ and a range of $\mathcal{M}_\infty$ and corresponding ϵ_ρ values. In Figure 4 models from Table 1 are presented, which have $\gamma = \Gamma_s = 4/3$, while in Figure 5 models from Table 2 are presented, which have $\gamma = \Gamma_s = 5/3$. In these slices, the x- and y-axes show distances in units of the accretion radius R_a, and we overplot streamlines of the velocity field within the x–y plane.

Higher Mach numbers imply steeper density gradients relative to the accretion radius, following Equation (11). These conditions tend to be found in the outer regions of the stellar envelope, whereas lower Mach numbers and shallower density gradients are more representative of flows found deeper in the stellar envelope. Thus, the sequence of Mach numbers approximates the inspiral of an object from the outer regions of the envelope of the donor star toward its center.

Figures 4 and 5 demonstrate how a decreasing $\mathcal{M}_\infty$ for fixed q_r affects the flow characteristics. A key distinction is that the flow symmetry is more dramatically broken at high $\mathcal{M}_\infty$ (and ϵ_ρ), and it gradually becomes more symmetric with decreasing $\mathcal{M}_\infty$ and ϵ_ρ (MacLeod & Ramirez-Ruiz 2015a; MacLeod et al. 2017). It is important to emphasize that the controlling parameter generating this asymmetric flow is the density gradient, rather than the Mach number itself. In the highly asymmetric cases, the dense material from negative y values does not stagnate at $y = 0$, as in the canonical HL flow. Instead, this material pushes its way to positive y values (where the background density is lower), as it is deflected by the gravitational influence of M_2. In the cases where $\mathcal{M}_\infty = 1.15$, the flow is nearly symmetric, as density gradients are quite mild and the flow morphology approaches that of the classic HL case.

The bottom panels of Figures 4 and 5 show slices of flow Mach number near the embedded object. In case of the high upstream Mach numbers or steeper upstream density gradients, most of the material in the post-shock region is supersonic, with a negligible amount of material having $\mathcal{M} \ll 1$ values. As the upstream Mach number is decreased, or the upstream density gradient is made shallower, the bow shock becomes more symmetric. The upstream flow is supersonic, whereas after the material crosses the shock and meets the pressure gradient caused by the convergence of the flow in the post-shock region, the downstream flow becomes subsonic. In Figure 4, for the lowest upstream Mach number case in the $\gamma = 4/3$ simulations, we observe a sonic surface in the Mach number plot, crossed by red post-shock material, as it transitions to blue (supersonic) infall toward the sink. For the $\gamma = 5/3$ simulations, this feature is not visible, as the sonic point is located at the accretor (at zero radius).

We can anticipate the implications of these flow distributions on coefficients of accretion and drag. With increasing $\mathcal{M}_\infty$, the disturbance in the flow symmetry is expected to reduce the rate of accretion: streamlines show that less material is converging toward the embedded object. We also note that for larger density gradients (higher $\mathcal{M}_\infty$) the post-shock flow is generally more turbulent, and the rate of accretion of material into the sink becomes more variable. The variation of density flowing within the accretion radius in the high-$\mathcal{M}_\infty$ cases cause dense material from negative y regions to be focused into the object's wake, which might be expected to enhance the dynamical friction drag force.

3.4.2. Dependence on Mass Ratio, q_r

Varying mass ratio can be representative of differing binary initial conditions, or even changing enclosed mass within a given binary. Figure 6 shows slices of density through the orbital (x–y) plane from the simulations performed for q_r values

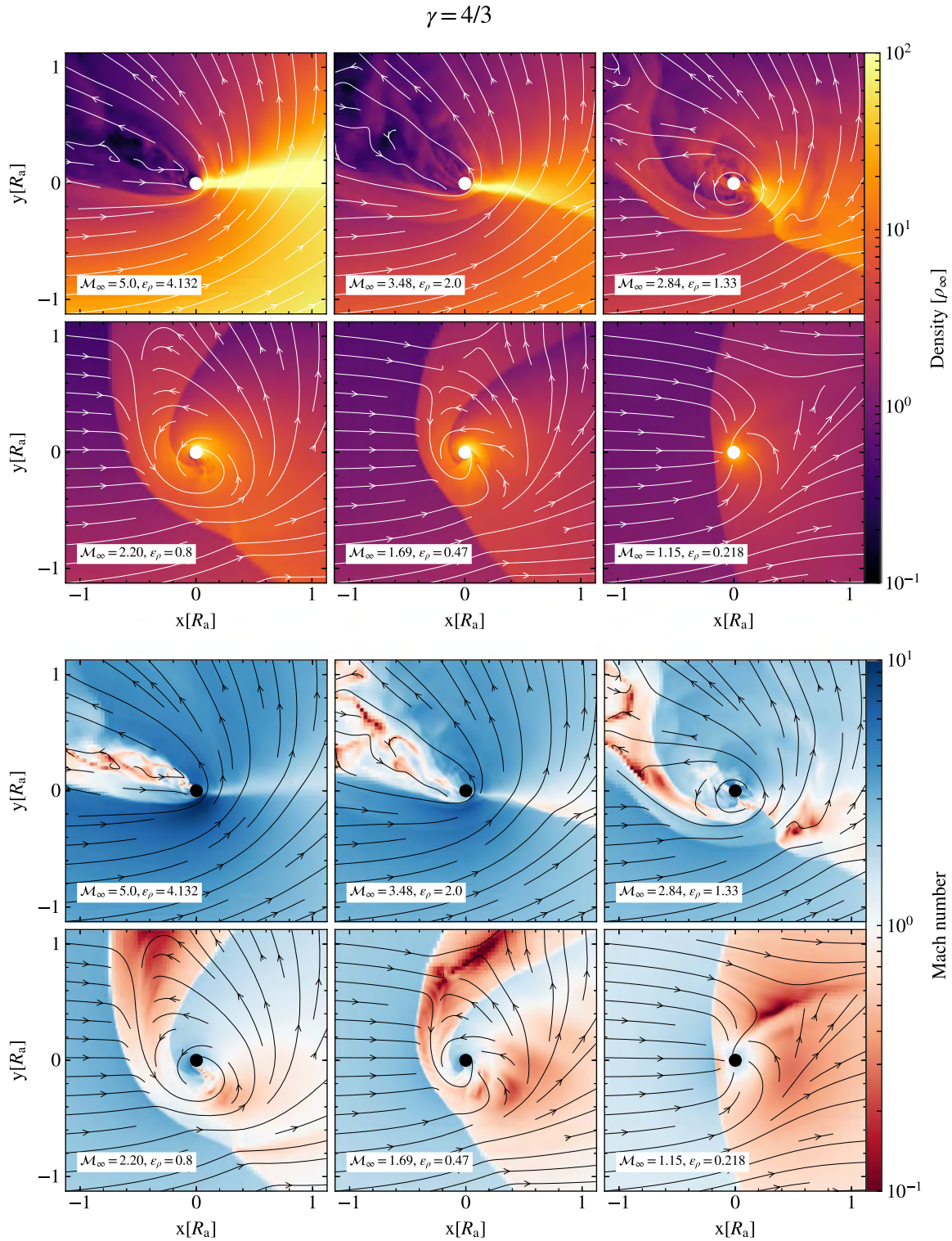

Figure 4. Slices of density in units of ρ_∞ (top panels) and Mach number (bottom panels) through the orbital (x–y) plane, for a fixed mass ratio q_r and varying upstream Mach number $\mathcal{M}_\infty$, for the simulation suite $(\Gamma_s, \gamma) = (4/3, 4/3)$. The simulations use $q_r = 0.1$ and $\mathcal{M}_\infty$ 5.0, 3.48, 2.84, 2.20, 1.69, and 1.15, corresponding to density gradients ϵ_ρ of 4.132, 2.0, 1.33, 0.8, 0.47, and 0.218, respectively. The slices compare the state of the flow at simulation time $t = 30R_a/v_\infty$. Moving from the highest to the lowest $\mathcal{M}_\infty$, the slices show the pattern of the flow around the embedded companion object as it inspirals from the outer to the inner regions of the primary star's envelope.

$1/10$ and $1/3$ and a fixed $\mathcal{M}_\infty = 1.15$ for both $\gamma = \Gamma_s = 4/3$ and $\gamma = \Gamma_s = 5/3$.

Comparison of the panels of Figure 6 demonstrates the effect of q_r on the flow characteristics. Although $\mathcal{M}_\infty$ is held constant, the corresponding ϵ_ρ is largest in the $q_r = 1/3$ case and smallest for $q_r = 1/10$, as shown in Tables 1 and 2. This yields the most obvious difference with varying q_r: the flow in the $q_r = 1/3$ case is more asymmetric (e.g., the bow shock is

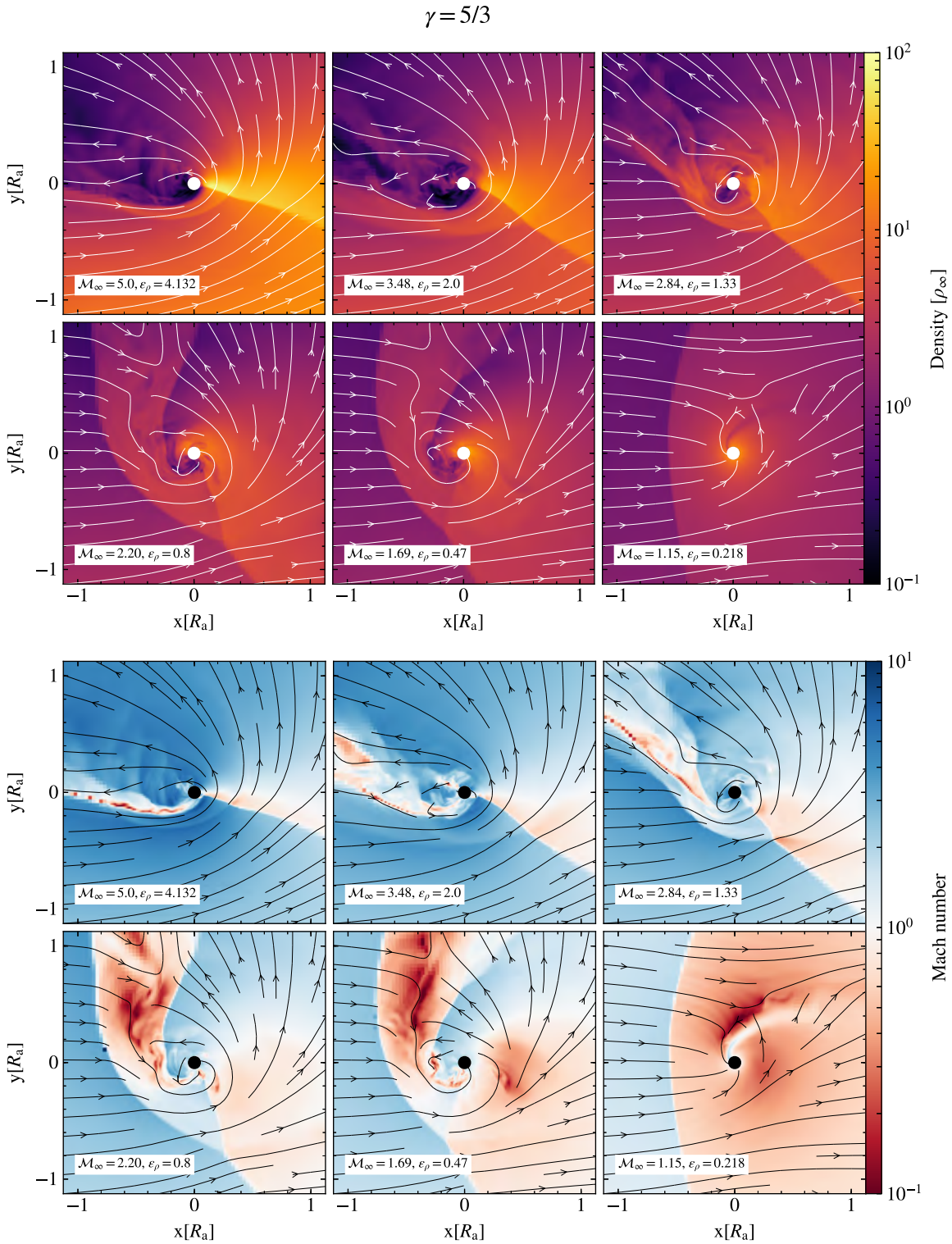

Figure 5. Slices of density in units of ρ_∞ (top panels) and Mach number (bottom panels) through the orbital (x–y) plane, for a fixed mass ratio q_r and varying upstream Mach number $\mathcal{M}_\infty$, for the simulation suite $(\Gamma_s, \gamma) = (5/3, 5/3)$. The simulations use $q_r = 0.1$ and $\mathcal{M}_\infty$ 5.0, 3.48, 2.84, 2.20, 1.69, and 1.15, corresponding to density gradients ϵ_ρ of 4.132, 2.0, 1.33, 0.8, 0.47, and 0.218, respectively. The slices compare the state of the flow at simulation time $t = 30R_a/v_\infty$. Moving from the highest to the lowest $\mathcal{M}_\infty$, the slices show the pattern of the flow around the embedded companion object as it inspirals from the outer to the inner regions of the primary star's envelope.

more distorted) as a result of the stronger density gradient. Second, we observe that the higher-q_r cases have weaker focusing of the flow around the embedded object, as evidenced by the pre-shock flow streamlines. This happens because as the mass ratio increases, from Equation (6), R_a/a increases. We choose our model domain sizes to capture this difference in scales, as described in Section 3.1. When the accretion radius is a larger fraction of the orbit size, gravitational focusing acts over fewer characteristic lengths R_a to concentrate the flow. One implication is that the effective interaction cross section is

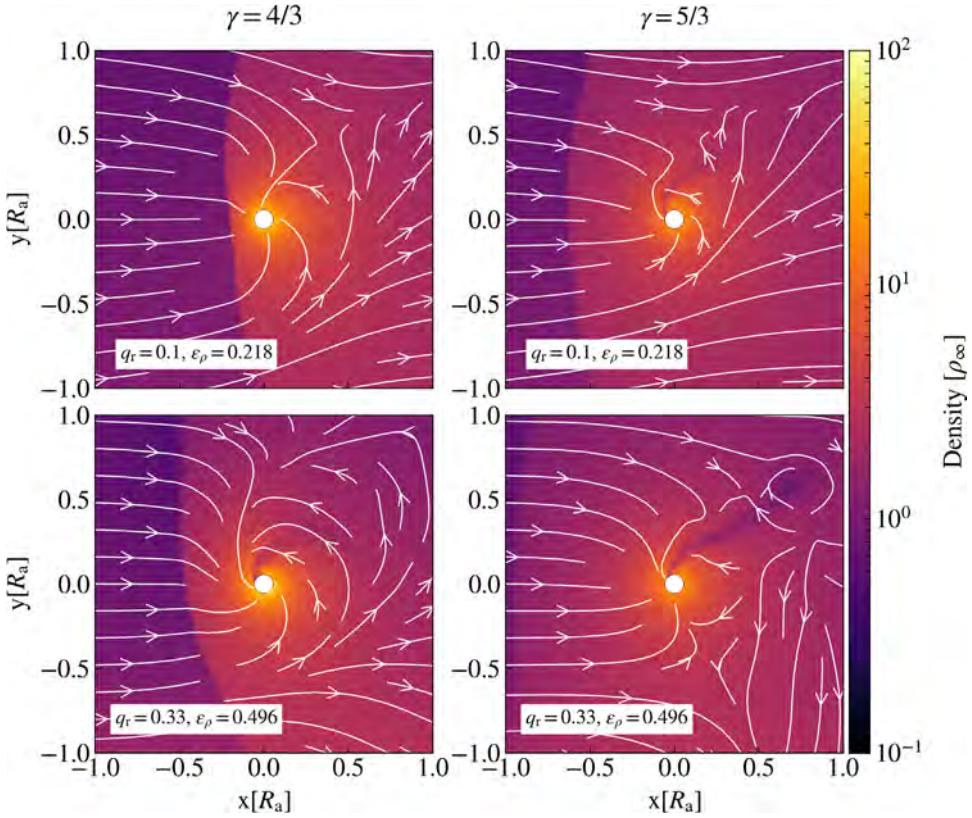

Figure 6. Slices of density in units of ρ_∞ for the simulation suite $(\Gamma_s, \gamma) = (4/3, 4/3)$ (left panels) and for the simulation suite $(\Gamma_s, \gamma) = (5/3, 5/3)$ (right panels) through the orbital (x–y) plane, for a fixed upstream Mach number $\mathcal{M}_\infty$ and varying ratio q_r. The simulations for each γ use $\mathcal{M}_\infty = 1.69$ and $q_r = 0.1$ (top) and 0.33 (bottom). The slices compare the state of the flow at simulation time $t = 30R_a/v_\infty$. The panels show the dependence of the flow pattern around the embedded companion object in a specific region of the envelope on the binary mass ratio.

smaller than πR_a^2, because the original HL derivation of R_a assumes a ballistic trajectory focused from infinite distance.

Therefore, with increasing q_r, we anticipate a decrease in the dynamical friction drag force due to the smaller effective cross section. The implications for the accreted mass are less obvious from these slices because the morphology of the post-shock flow is largely similar owing to the competition between steeper density gradients but smaller effective cross sections at larger q_r.

3.4.3. Dependence on Adiabatic Index, γ

Here we examine the dependence of flow properties on the stellar envelope equation of state, using two limiting cases of ideal gas equations of state that bracket the range of typical stellar envelope conditions. A $\gamma = 4/3$ equation of state is representative of a radiation-pressure-dominated equation of state, occurring in massive-star envelopes, or in zones of partial ionization in lower-mass stars. A $\gamma = 5/3$ equation of state represents a gas-pressure-dominated equation of state, as occurs in the interiors of relatively low mass stars with masses less than approximately $8M_\odot$ (e.g., MacLeod et al. 2017; Murguia-Berthier et al. 2017). Values between these limits are also possible, dependent on the microphysics of the density–temperature regime (Murguia-Berthier et al. 2017).

While there are many similarities in overall flow morphology in our simulation suites A (Table 1) and B (Table 2), because gas is less compressible with $\gamma = 5/3$ than it is with $\gamma = 4/3$, there are several key differences between these two cases. Gas near the accretor tracks closer to ballistic, rotationally supported trajectories in the $\gamma = 4/3$ case, as compared to the less compressible $\gamma = 5/3$ case. A related feature is that the bow shock stands farther off from the accretor into the upstream flow when $\gamma = 5/3$ than $\gamma = 4/3$. These properties are visible when comparing the equivalent panels of Figures 5 and 4, or the left and right panels of Figure 6. The underlying explanation is similar: shock structures around the accretor are set by the balance of the gravitational attraction of the accretor, the ram pressure of incoming material, and pressure gradients that arise as gas is gravitationally focused. For the less compressible $\gamma = 5/3$ models, gas pressure gradients exceed the accretor's gravity and partially prevent accretion. We observe the consequence of this in lower-density voids of hot, low Mach number material in Figure 5. For the more compressible $\gamma = 4/3$ flow, gas is more readily compressed, and pressure gradients build at a similar rate to the gravitational force (Murguia-Berthier et al. 2017). One consequence of this is that higher densities near the accretor track the compression of gas deep into the accretor's gravitational potential well.

3.5. Coefficients of Drag and Accretion

We now use the results from the wind tunnel experiments to understand the effects of q_r and $\mathcal{M}_\infty$ on the accretion of material onto the embedded object and on the drag force acting on the embedded object. Figure 7 shows median values of C_a and C_d computed over simulation times $10R_a/v_\infty < t < 30R_a/v_\infty$, as a function of $\mathcal{M}_\infty$ for different values of q_r. We use contributions from both the dynamical friction drag force, F_{df}, and the force due to linear momentum accretion $F_{\dot{p}_x}$ in calculating C_d (Equation (15)). In all our simulations, F_{df} is larger than $F_{\dot{p}_x}$;

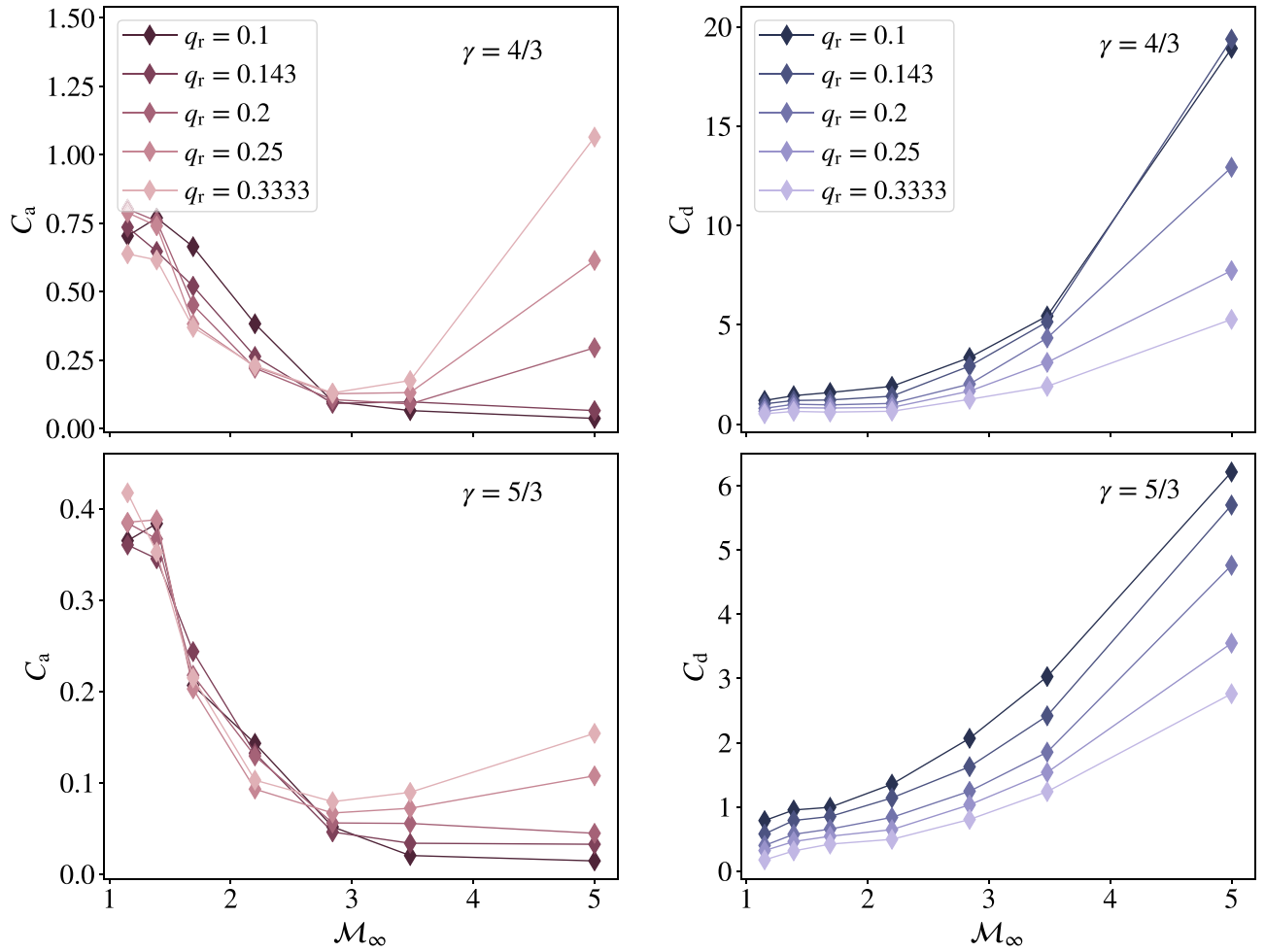

Figure 7. Variations of the median coefficient of accretion C_a and the median coefficient of drag C_d vs. upstream Mach number $\mathcal{M}_\infty$ for the $(\Gamma_s, \gamma) = (4/3, 4/3)$ simulations (top panels) and $(\Gamma_s, \gamma) = (5/3, 5/3)$ simulations (bottom panels). C_a (C_d) vs. $\mathcal{M}_\infty$ curves are shown for each q_r value at which simulations are performed. C_a is obtained by normalizing the mass accretion rate in the system to the HL theory mass accretion rate. C_d is obtained by normalizing the drag force in the system to the HL theory drag force. The C_a and C_d median values are computed in the simulation time range $10R_a/v_\infty < t < 30R_a/v_\infty$. For a fixed, small mass ratio q_r, a higher $\mathcal{M}_\infty$ corresponds to a steeper upstream density gradient that breaks the symmetry of the flow, causing a reduction in C_a, and a greater quantity of dense material gravitationally focused from the deep stellar interior, which increases C_d.

however, as we find in Section 4.1, the sum of these forces is the quantity that is invariant with respect to changing the numerical parameter of sink radius.

In Appendix A, we present fitting formulae for the coefficients of accretion C_a and drag force C_d as a function of the mass ratio and Mach number from both our $\gamma = 4/3$ and $\gamma = 5/3$ simulations, showing the mapping between the $(q_r, \mathcal{M}_\infty) \rightarrow (C_a, C_d)$ parameter space that we have explored.

3.5.1. Dependence on Mach Number, $\mathcal{M}_\infty$

We begin by examining the dependence of drag and accretion coefficients with upstream Mach number, $\mathcal{M}_\infty$. Figure 7 shows that for $\mathcal{M}_\infty \lesssim 3$, at fixed q_r, C_a decreases with increasing $\mathcal{M}_\infty$. For $q_r \lesssim 0.2$, this trend continues to higher $\mathcal{M}_\infty$, while for $q_r \gtrsim 0.2$, the coefficient of accretion rises again with increasing $\mathcal{M}_\infty$, particularly in the $\gamma = 4/3$ models. This general trend can be understood in the context of the associated density gradients. For fixed q_r, higher-$\mathcal{M}_\infty$ flows correspond to steeper density gradients relative to the accretion radius. The steep density gradient breaks the symmetry of the post-shock flow, as discussed in Section 3.4.1. The resulting net rotation and angular momentum act as a barrier to accretion and lead to a drop in the accretion rate as compared to the HL rate ($\pi R_a^2 \rho_\infty v_\infty$; MacLeod & Ramirez-Ruiz 2015a). The increase in C_a for large q_r at high $\mathcal{M}_\infty$ runs counter to this overall trend. In these cases, the combined steepening of the density gradient and weakening of the overall gravitational focus and slingshot discussed in Section 3.4.2 lead to a flow morphology that very effectively transports dense material from $-y$ impact parameters toward the sink, instead of imparting so much angular momentum that it is flung to $+y$ coordinates, resulting in large C_a.

As for the drag force, we see that for each value of q_r, C_d monotonically increases by a factor of $\mathcal{O}(10)$ with increasing $\mathcal{M}_\infty$ across the range of $\mathcal{M}_\infty$ values for which we have performed simulations. This trend reflects the fact that higher local gas densities, ρ, are achieved within the accretion radius of M_2 for higher values of the upstream Mach number, $\mathcal{M}_\infty$. This higher-density material ($\rho \gg \rho_\infty$) focused into the wake of the embedded object from deeper inside the interior of the primary star enhances the dynamical friction drag force as compared to the HL drag force ($\pi R_a^2 \rho_\infty v_\infty^2$).

3.5.2. Dependence on Mass Ratio, q_r

For each $\mathcal{M}_\infty$, we can also see the dependence of C_a and C_d on the mass ratio q_r in Figure 7. As the mass ratio increases, the accretion radius becomes a larger fraction of the orbit size. This causes the flows to be focused from a distance that is a smaller multiple of the accretion radius, causing weaker focusing and gravitational slingshot of the gas, as discussed in Section 3.4.2. The effect of this difference on the coefficients of accretion at $\mathcal{M}_\infty \lesssim 3$ is minimal. However, as discussed above in Section 3.5.1, at higher $\mathcal{M}_\infty$, there is a dramatic increase in C_a with increasing q_r that results in the capture of dense material from $-y$ impact parameters that does not possess sufficient momentum to escape the accretor's gravity.

In the higher-q_r cases, there is relatively weak momentum transfer to the gas. This weakens the drag forces relative to the HL drag force, which reduces the deceleration of the object. In Section 3.4.2, we discussed this effect in terms of a reduced effective cross section. In terms of the coefficients of drag in Figure 7, the quantitative effects are particularly clear. When gas is gravitationally focused over fewer characteristic length scales (because R_a is a larger fraction of a at larger q_r), we see lower dimensionless drag forces, C_d.

3.5.3. Dependence on Adiabatic Index, γ

The gas adiabatic index has important consequences for coefficients of drag and accretion because while pressure gradients enter into the fluid momentum equation, distributions of gas densities set rates of drag and accretion. Thus, the equation of state is crucial both for the flow morphology, as discussed in Section 3.4.3, and for C_a and C_d.

In Figure 7 we note that the increased resistance to compression by the accretor's gravitational force of the $\gamma = 5/3$ models leads to lower C_a by a factor of approximately 2 than the equivalent $\gamma = 4/3$ models. We saw the effects of this in the density slices of Figures 4 and 5, in which the material in the vicinity of M_2 is not as dense in the $\gamma = 5/3$ models as it is in the $\gamma = 4/3$ simulations. Second, the larger pressure support provided by the gas in the $\gamma = 5/3$ simulations decreases the overdensity of the post-shock wake versus what is realized in the simulations with $\gamma = 4/3$. The greater upstream-downstream symmetry that results decreases the net dynamical friction force exerted on the embedded object. We observe that C_d is approximately a factor of 3 lower for $\gamma = 5/3$ than $\gamma = 4/3$ in the right panels of Figure 7.

Having explored the parameter space of gas flow and coefficients of gas and accretion in our wind tunnel models, in the following section we explore the application of these results to astrophysical common envelope encounters. In Appendix B, we compare the drag forces measured in this work with other approaches to measure drag forces in common envelope encounters.

4. Accretion onto Black Holes during a Common Envelope Inspiral

In this section we discuss the application of our wind tunnel results to the scenario of a black hole dynamically inspiraling through the envelope of its companion. We focus in particular on the accreted mass and spin, because these parameters directly enter into the gravitational-wave observables. To do so, we discuss the application and extrapolation of our numerical measurements of C_a and C_d to black holes and the implications on the accreted mass and spin for LIGO-Virgo's growing binary black hole merger population.

4.1. Projected Accretion and Drag Coefficients for Compact Objects

A limitation of our numerical models is that the accretion rate and, to a lesser extent, the drag force have been shown to depend on the size of the central absorbing sink (see Ruffert 1994, 1995; Ruffert & Arnett 1994; Blondin & Raymer 2012; MacLeod & Ramirez-Ruiz 2015a; Antoni et al. 2019). This dependence indicates that results do not converge to a single value regardless of the numerical choice of sink radius, R_s. Further, simultaneously resolving the gravitational focusing radius, R_a, and the size of a compact object is currently not computationally feasible: R_a might be on the order of the envelope radius, while an embedded compact object's radius is orders of magnitude smaller still. Previous work by MacLeod & Ramirez-Ruiz (2015a, 2015b) and MacLeod et al. (2017) has pointed out that these limitations make accretion coefficients derived from simulations at most upper limits on the realistic accretion rate.

Here we attempt to systematically explore the scaling of coefficients of accretion and drag to smaller sink radii, which is smaller R_s/R_a values. We ran two additional sets of 35 models that reproduce models A1 through A35, reducing the sink radius by a factor of two to $R_s/R_a = 0.025$ and $R_s/R_a = 0.0125$. To preserve the same level of resolution across the sink radius, we add an additional layer of mesh refinement around the sink with each reduction of sink radius (effectively halving the minimum zone width). From these models, we measure coefficients of drag and accretion following the methodology identical to our standard models presented earlier.

With accretion and drag coefficients derived across a factor of four in sink radius, we fit the dependence on sink radius with power laws of the form

$$\log_{10}(\dot{M}) = \alpha_{\dot{M}} \log_{10}(R_s/R_a) + \beta_{\dot{M}} \tag{16}$$

$$\log_{10}(F_d) = \alpha_F \log_{10}(R_s/R_a) + \beta_F. \tag{17}$$

Thus, $\dot{M} \propto (R_s/R_a)^{\alpha_{\dot{M}}}$ and $F_d \propto (R_s/R_a)^{\alpha_F}$. With these coefficients, we have some indication of how rates of accretion and drag forces might extrapolate to much smaller R_s/R_a that are astrophysically realistic.

Figure 8 presents the exponents of the power-law relations of the accretion rate and drag force on the sink radius, as a function of $\mathcal{M}_\infty$. For each (q_r, $\mathcal{M}_\infty$) model, there are three sets of (C_a, C_d) values from the $R_s/R_a = [0.0125, 0.025, 0.05]$ simulations, respectively. A linear least-squares fit of Equation (16) to the three C_a values is performed. The slope of the fitted line is $\alpha_{\dot{M}}$, which is the exponent of the power-law function relating $\dot{M}$ to R_s/R_a. Similarly, a linear least-squares fit of Equation (17) to the three C_d values is used to derive α_F, the exponent of the power-law function relating F_d to R_s/R_a. Thus, we derive one $\alpha_{\dot{M}}$ and one α_F (represented with crosses in Figure 8) per (q_r, $\mathcal{M}_\infty$) model. We observe that the majority of the $\alpha_{\dot{M}}$ values are positive, indicating that accretion rates drop as sink sizes get smaller relative to R_a. Additionally, we observe that $\alpha_{\dot{M}}$ is typically lower in low Mach number flows, $\mathcal{M}_\infty \lesssim 2$, which have proportionately shallower density gradients. Above $\mathcal{M}_\infty \gtrsim 2$, $\alpha_{\dot{M}}$ is approximately constant with increasing $\mathcal{M}_\infty$. At a given $\mathcal{M}_\infty$, there is variation between the models, depending on the mass ratio, q_r. However, for simplicity, the following piecewise linear plus constant least-squares fit

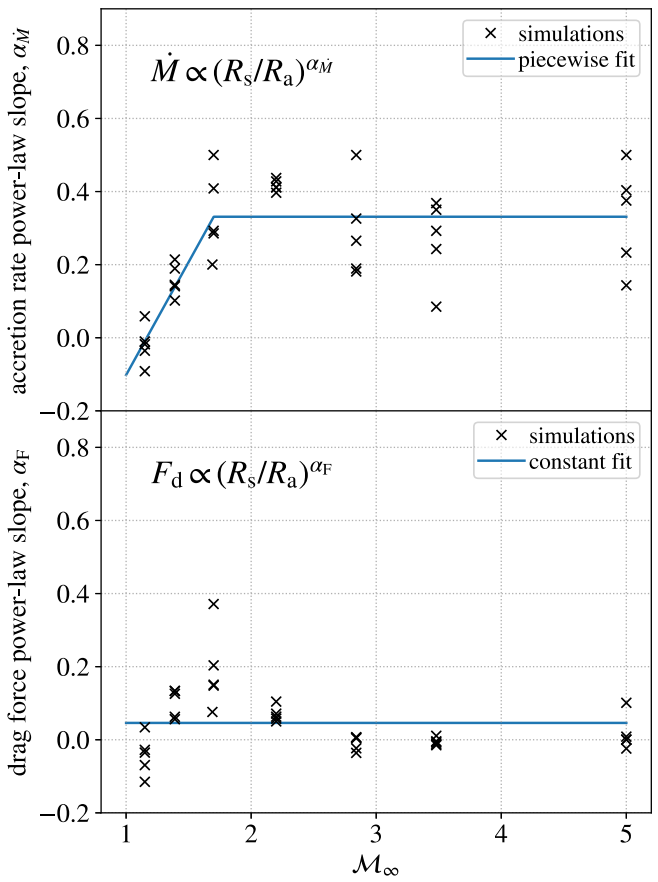

Figure 8. Exponents of power-law relations of the accretion rate, $\alpha_{\dot{M}}$, and drag force, α_F, on the sink radius. Top panel: for each $\gamma = 4/3$ simulation in Table 1, an $\alpha_{\dot{M}}$ (denoted by a cross) is derived from a linear least-squares fit of Equation (16) to the C_a value measured from that simulation of sink size $R_s = 0.05\ R_a$, plus similar simulations with $R_s = [0.025, 0.0125]\ R_a$. The plot shows a largely positive $\alpha_{\dot{M}}$, which indicates that accretion rates decrease as sink size decreases. The blue line shows a fit to the dependence of $\alpha_{\dot{M}}$ on $\mathcal{M}_\infty$, using the piecewise fitting relation given by Equation (18). Bottom panel: Following the same procedure for calculating $\alpha_{\dot{M}}$, each α_F (denoted by a cross) value is derived from a linear least-squares fit of Equation (17) to C_d values from simulations of varying sink sizes. The plot shows values of $\alpha_F \sim 0$, indicating little change in the overall drag force as the sink radius is modified. The blue line shows α_F across $\mathcal{M}_\infty$ values using a constant least-squares fit, which gives $\alpha_F \approx 0.05$.

(blue line in Figure 8) reproduces the main trends

$$\alpha_{\dot{M}} \approx \begin{cases} 0.62\mathcal{M}_\infty - 0.72, & \mathcal{M}_\infty < 1.7, \\ 0.33, & \mathcal{M}_\infty \geqslant 1.7. \end{cases} \tag{18}$$

By comparison, exponents of power-law dependence of the drag coefficients on sink radius, α_F, do not show particularly structured behavior with $\mathcal{M}_\infty$. Further, most values are near zero, with all but one model lying within $-0.2 < \alpha_F < 0.2$. Least-squares fitting of a constant finds $\alpha_F \approx 0.05$, which is close to 0. This indicates that there is little change in the drag force with changing sink size.

Taken together, these scalings indicate that when $R_s/R_a \ll 1$, we can expect drag forces to remain relatively unchanged while accretion rate decreases. As a specific example, if an accreting black hole has $R_s/R_a = 10^{-5}$ at $\mathcal{M}_\infty = 2$, our scaling above suggests that we can expect the realistic accretion coefficient to be approximately 6% of the value derived in our simulations with $R_s/R_a = 0.05$ (because $(10^{-5}/0.05)^{0.33} \approx 0.06$). This result makes intuitive sense in light of our simulation results: drag forces arise from the overdensity on the scale of R_a, while, especially in the higher-$\mathcal{M}_\infty$ (higher-ϵ_ρ) cases, rotation inhibits radial, supersonic infall of gas to the smallest scales.

4.2. Coupled Orbital Tightening and Accretion

As a black hole spirals through the common envelope gas, its orbit tightens in response to drag forces, and it may also potentially accrete mass from its surroundings. Under the HL theory of mass accretion and drag, the degree of mass growth is coupled to the degree of orbital tightening. Thus, a given orbital transformation is always accompanied by a corresponding mass change in this theory. Chevalier (1993), Brown (1995), and Bethe & Brown (1998) elaborated on this argument and suggested that compact objects in common envelope phases might easily double their masses.

Here we reexpress this line of argument with the addition of separate coefficients of drag and accretion (which might, for example, be motivated by numerical simulations). Orbital energy, $E = -GM_1M_2/2a$, is dissipated by the drag force at a rate $\dot{E} = -Fv$ (if force is defined positive, as in our notation). Expressed in terms of the coefficient of drag, $\dot{E} = -C_d F_{HL} v = -C_d \dot{M}_{HL} v^2 = -C_d \dot{E}_{HL}$ (Equations (3) and (4)). We will approximate the relative velocity here as the Keplerian velocity, such that $v^2 \approx G(M_1 + M_2)/a$. We can then write the mass gain per unit orbital energy change,

$$\begin{aligned} \frac{dM_2}{dE} = \frac{\dot{M}}{\dot{E}} &= -\frac{C_a \dot{M}_{HL}}{C_d \dot{M}_{HL} v^2} = -\frac{C_a}{C_d v^2}, \\ &= \frac{1}{2(1+q_r)} \frac{M_2}{E} \frac{C_a}{C_d}, \end{aligned} \tag{19}$$

or equivalently,

$$\frac{d \ln M_2}{d \ln E} = \frac{1}{2(1+q_r)} \frac{C_a}{C_d}. \tag{20}$$

This implies that the mass gained by the embedded, accreting compact object is related to the reduced mass of the pair and the ratio of accretion to drag coefficients. We can integrate this equation under the approximation that q_r, C_a, and C_d remain close to typical values, which we denote $\overline{C_a}$, $\overline{C_d}$, and $\overline{q_r}$, over the course of the inspiral from the onset of common envelope evolution through envelope ejection. In this approximation,

$$\frac{M_{2,f}}{M_{2,i}} \approx \left(\frac{E_f}{E_i}\right)^{\left(\frac{1}{2(1+\overline{q_r})}\frac{\overline{C_a}}{\overline{C_d}}\right)}. \tag{21}$$

We can therefore conclude that if $\overline{C_a} = \overline{C_d} = 1$, the fractional change in the mass of the embedded object is on the order of the square root of the change in the orbital energy, i.e., binary separation (Chevalier 1993; Brown 1995; Bethe & Brown 1998).

If accreted material carries net angular momentum, a black hole will also accrue spin. Assuming an initially nonspinning black hole, the accrued spin can be written in terms of $\Delta M_2/M_{2,i}$. The highest spins are achieved if material accretes with the specific angular momentum of the last stable circular orbit and uniform direction. In this case, the final spin is

$$\chi = \sqrt{\frac{2}{3}} X (4 - \sqrt{18X^2 - 2}), \tag{22}$$

where $X = 1/(1 + \Delta M_2/M_{2,i})$ (King & Kolb 1999). Under these assumptions, the dimensionless spin reaches unity when $X = 1/\sqrt{6}$ or $\Delta M/M_{2,i} \approx 1.4$ (as shown in Figure 1 of King & Kolb 1999).

From these arguments, we see that the ratio of accretion to drag coefficient is crucial in determining the accrued mass and spin onto a compact object. In the HL formalism, in which $\overline{C_a} = \overline{C_d} = 1$, and the accreted mass is given by Equation (21), for $\overline{q_r} = 0.1$, we find that $\chi \to 1$ for $E_f/E_i \gtrsim 7$.

4.3. Implications for Common Envelope Transformation of Black Holes and Gravitational-wave Observables

In Figure 9 we show the ratio of the coefficients of drag and accretion derived in our simulations. For illustrative purposes, we also scale these values using the power-law slopes derived in Section 4.1 to a much smaller sink radius, $R_s/R_a = 10^{-5}$. This is, for example, appropriate for a $5M_\odot$ black hole (with horizon radius of approximately 1.5×10^6 cm) embedded deep within a $30M_\odot$ primary-star envelope at a separation of $10R_\odot$. Then, $q_r = 1/6$ and $R_a/a \approx 0.3$, from Equation (6). Thus, $R_a \approx 2 \times 10^{11}$ cm, and $R_s/R_a \sim 10^{-5}$. However, we note that for larger separations, even smaller R_s/R_a will be appropriate.

We observe that for the majority of the $q_r - \mathcal{M}_\infty$ parameter space, $C_a/C_d \ll 1$, even in the direct simulation coefficients, though C_a/C_d approaches unity as $\mathcal{M}_\infty \to 1$. For specificity, if we use our direct (unscaled) simulation coefficients and take the example case of a black hole involved in a $\overline{q_r} \sim 0.1$ encounter, $C_a/C_d \lesssim 0.1$ for $\mathcal{M}_\infty \gtrsim 2$. This is the bulk of the relevant parameter space for a dynamical inspiral if the relative velocity between the black hole and the envelope gas is similar to the Keplerian velocity (see Figures 3 and 4 of MacLeod & Ramirez-Ruiz 2015a and Figure 1 of MacLeod et al. 2017). If $C_a/C_d = 0.1$, then $d \ln M_2 / d \ln E \approx 0.045$ (Equation (20)), i.e., a 5% change in the mass of the black hole due to accretion per orbital e-folding during the common envelope encounter. If this accreted mass is coherently maximally rotating, the black hole would spin up to $\chi \sim 0.15$ (if it begins with $\chi = 0$). Thus, if the orbital energy changes by a factor of 25, the black hole would accrete about 15% of its original mass (Equation (21)) and spin up to $\chi \sim 0.4$ (Equation (22)).

However, we have argued in Section 4.1 that the simulated C_a/C_d can be misleadingly high (or, alternatively, is best interpreted as a strict upper limit) because the compact-object radius is orders of magnitude smaller than R_s. With the rescaled results of the second panel of Figure 9 for $R_s = 10^{-5}R_a$, we see that for the same $\overline{q_r} = 0.1$ encounter in which $\mathcal{M}_\infty \gtrsim 2$, the ratio of the accretion to drag coefficient is $C_a/C_d \lesssim 10^{-2}$. This in turn implies that a black hole undergoing such a common envelope encounter accretes according to $d \ln M_2 / d \ln E \approx 0.0045$. Again, taking the example of orbital energy changing by a factor of 25, the black hole would accrete 1.4% of its own mass and spin up to $\chi \sim 0.05$. Even if the binary hardens by three orders of magnitude during the common envelope phase, a nonspinning black hole would only accrete ~3% of its original mass and spin up to $\chi \sim 0.1$.

A possible exception to these predictions of low accreted mass and spin are black holes embedded in $\mathcal{M}_\infty \sim 1$ flows (involving dense stellar envelope material) and proportionately shallow density gradients. In these cases black holes can accrete at similar to the HL rate, largely because the environment is nearly homogeneous on the scale of R_a. This regime of Mach numbers may be relevant to the self-regulated common envelope inspiral phase that follows the dynamical inspiral. However, in this case, Mach numbers are lower in part because the embedded objects interact with much lower density, higher entropy gas as the orbit starts to stabilize (e.g., Ivanova & Nandez 2016; Ohlmann et al. 2016a; Iaconi et al. 2018; Chamandy et al. 2019a). This is presented quantitatively in the study by Chamandy et al. (2019a) of forces during a common envelope simulation, which showed that forces significantly decrease below those expected from the original stellar profile as the orbit stabilizes.

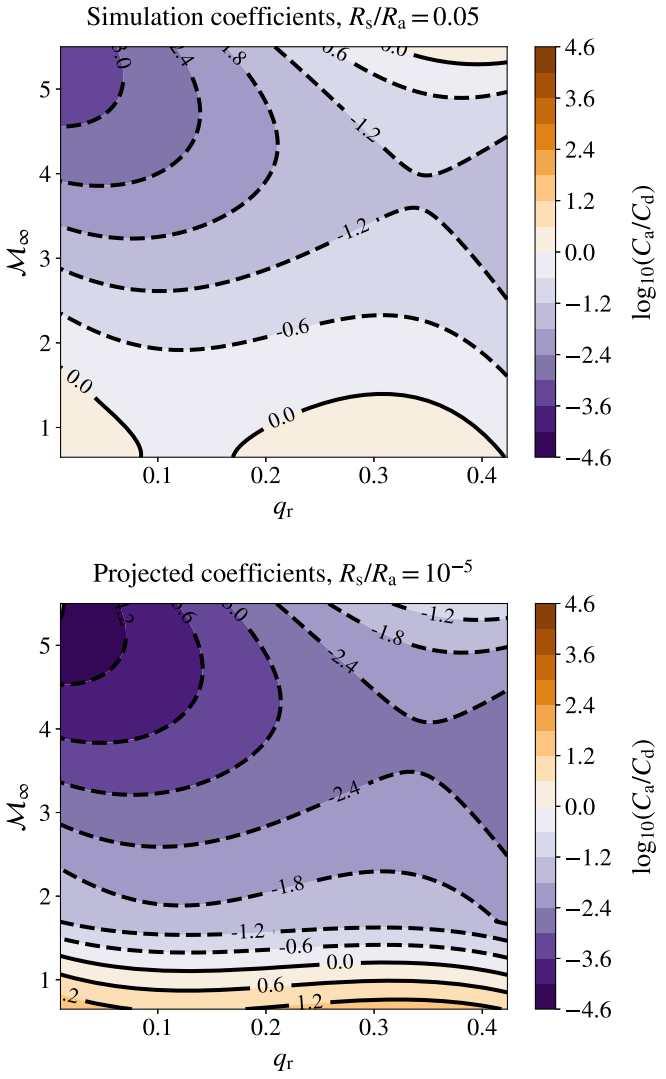

Figure 9. Two-dimensional contour plot of $\log_{10}(C_a/C_d)$ in the $q_r - \mathcal{M}_\infty$ space using numerical results from the $\gamma = 4/3$ simulations presented in this paper. The top panel shows the $(q_r, \mathcal{M}_\infty) \to (C_a, C_d)$ mapping for the sink size used in the simulations $R_s/R_a = 0.05$. The bottom panel shows the $(q_r, \mathcal{M}_\infty) \to (C_a, C_d)$ mapping with the coefficients extrapolated to a sink size $R_s/R_a = 10^{-5}$, which is more realistic for a black hole embedded in a common envelope.

The current catalog of gravitational-wave events observed by the LIGO-Virgo detectors demonstrates the existence of moderately massive black holes in binary systems (Abbott et al. 2016a, 2016b, 2017a, 2017b, 2017c, 2019; Biwer et al. 2019; De et al. 2019; Nitz et al. 2019, 2020; Venumadhav et al. 2020; Zackay et al. 2019). Common envelope evolution is considered to be one of the preferred channels for the formation of these binaries (Belczynski et al. 2016; Eldridge & Stanway 2016; Kruckow et al. 2016; Stevenson et al. 2017; Mapelli 2018).

These predictions therefore have important potential implications when considering the evolutionary history of the LIGO-Virgo network's growing population of gravitational-wave merger detections.

If the typical black hole passing through a common envelope phase accreted a significant fraction of its own mass and reached dimensionless spin near unity (as implied by Equations (21) and (22) if $C_a/C_d = 1$), this would have two directly observable consequences on the demographics of merging black holes. The mass gaps believed to exist in the birth distributions of black holes masses (Bailyn et al. 1998; Özel et al. 2010; Farr et al. 2011; Kreidberg et al. 2012; Yusof et al. 2013; Belczynski et al. 2014; Marchant et al. 2016; Woosley 2017) would be efficiently eradicated if black holes doubled their masses over the typical evolutionary cycle. Second, the average projected spins of merging black holes onto the orbital angular momentum would be large ($\chi_{\rm eff} \sim 1$ if coherently oriented) or at least broadly distributed (if randomly oriented), contrary to the existing interpretation of spins from LIGO-Virgo black hole observations (e.g., Farr et al. 2017, 2018; Tiwari et al. 2018; Piran & Piran 2020), or the predictions of spins in merging binary black holes (e.g., Kushnir et al. 2016; Schrøder et al. 2018; Zaldarriaga et al. 2018; Bavera et al. 2020; Batta & Ramirez-Ruiz 2019; Fuller & Ma 2019).

Our prediction of percent-level mass and spin accumulation yields a very different landscape of post−common envelope black holes. Our models suggest that common envelope phases should not significantly modify the natal masses or spins of black holes. If black holes are formed with nonsmooth mass distributions (including gaps or other features) or with low spin values, our models predict that these features would persist through a common envelope phase.

5. Conclusions

In this paper have we explored the effects of varying the binary mass ratio on common envelope flow characteristics, as well as coefficients of accretion and drag, using the common envelope wind tunnel setup of MacLeod et al. (2017). As the binary mass ratio is varied, the ratio of the gravitational focusing scale of the flow to the binary separation changes. We have also varied the flow upstream Mach number and gas adiabatic constant, which were investigated in MacLeod et al. (2017) and MacLeod & Ramirez-Ruiz (2015a). We have derived fitting formulae for the efficiency of accretion and drag from our simulations and have applied these to derive implications for the mass and spin accreted by black holes during the common envelope encounter. Some key conclusions of this work are as follows:

1. Using a systematic survey of the dimensionless parameters that characterize gas flows past objects embedded within common envelopes, we use our simplified common envelope wind tunnel hydrodynamic model to study the role of the upstream Mach number $\mathcal{M}_\infty$, enclosed mass ratio q_r, and the equation of state (as bracketed by adiabatic indices $\gamma = 4/3$ and $\gamma = 5/3$). For each model, we derive time-averaged coefficients of accretion, C_a, and drag, C_d (Tables 1 and 2).
2. Upstream Mach number $\mathcal{M}_\infty$ is a proxy for the dimensionless upstream density gradient ϵ_ρ (Equation (11)). Higher-$\mathcal{M}_\infty$ flows tend to have more asymmetric geometries owing to steeper density gradients (Figures 4 and 5). This transition in flow morphology is accompanied by higher drag coefficients but lower accretion coefficients (Figure 7).
3. The gas equation of state, parameterized here by the adiabatic index of ideal gas hydrodynamic models γ, primarily affects the concentration of gas flow around the accretor. When $\gamma = 5/3$, pressure gradients partially act against gravitational focusing (Figure 5 as compared to Figure 4) and reduce coefficients of both accretion and drag by a factor of a few relative to $\gamma = 4/3$ (Figure 7).
4. The binary mass ratio affects the ratio of gravitational focusing length to binary separation, R_a/a, shown in Equation (6) and Figure 1. As a result, larger mass ratio cases have weaker focusing of the flow around the embedded object, because gravitational focusing acts over a smaller number of gravitational focusing lengths to concentrate the flow (Figure 6). The consequences of this distinction are reduced drag (lower C_d) because of reduced momentum exchange with the flow, and, especially in the highest-$\mathcal{M}_\infty$ cases, higher capture fractions (increased C_a) because gas does not receive a sufficient gravitational slingshot to escape the accretor (Figure 7).
5. The size of a typical accretor is a factor of 10^3–10^8 times smaller than the gravitational focusing radius, R_a. Due to the limits of computational feasibility, our default numerical models adopt $R_s/R_a = 0.05$. We rerun the $\gamma = 4/3$ models with $R_s/R_a = 0.025$ and $R_s/R_a = 0.0125$. We find that drag coefficients are insensitive to R_s, but accretion coefficients have a dependence that we parameterize with a power-law slope, $\alpha_{\dot{M}}$ (Figure 8). These scalings allow us to extend our common envelope wind tunnel results to more astrophysically realistic scenarios.
6. The amount of mass accreted by a compact object during a common envelope phase is coupled to the degree of orbital tightening, as per the HL theory (Chevalier 1993; Brown 1995; Bethe & Brown 1998, and Section 4.2). Angular momentum carried by the accreted mass may also spin up the object. Therefore, the values of C_a and C_d are crucial in determining the mass and spin accrued by embedded objects during the common envelope phase (specifically, the ratio C_a/C_d sets the mass gain per unit orbital tightening, Equation (20)). In the HL scenario, where $C_a/C_d = 1$, the typical black hole immersed in a common envelope would gain on the order of its own mass and spin up to $\chi = 1$.
7. Our simulation results that $C_a/C_d \ll 1$ suggest that black holes spiraling in through common envelopes accumulate less than 1% mass per logarithmic change in orbital energy. In a typical event, this might correspond to a 1%–2% growth in black hole mass and spin up to a dimensionless spin of $\approx$0.05 for an initially nonspinning black hole (Figure 9 and Section 4.3). Thus, our predictions suggest that common envelope phases should not modify the mass and spin distributions of black holes from their natal properties.

The hydrodynamic models presented in this paper have numerous simplifications relative to the complex, time-dependent geometry and flow likely realized in a common envelope interaction. Nonetheless, they allow us to discover trends by systematically exploring the parameter space that may arise in typical interactions. A companion paper,

Everson et al. (2020), considers the stellar evolutionary conditions for donor stars in common envelope systems under which this dimensionless treatment is useful.

The ratio of accretion to drag coefficients (relative to their HL values) determines the amount of mass accretion during the dynamical inspiral phase of common envelope evolution. If our finding that $C_a/C_d \ll 1$ is correct, then the implications of this for gravitational-wave observables are significant. In particular, if the birth mass distributions of black holes have nonsmooth features, including gaps, or if black holes have low natal spins, these characteristic distributions will be preserved after the common envelope phase.

We gratefully acknowledge helpful discussions with A. Murgia-Berthier, P. Macias, A. Frank, E. Blackman, and D. Brown. We thank the Niels Bohr Institute for its hospitality while part of this work was completed, and we acknowledge the Kavli Foundation and the DNRF for supporting the 2017 Kavli Summer Program. S.D. received support for this work by the U.S. National Science Foundation grant PHY-1707954, the Inaugural Kathy '73 and Stan '72 Walters Endowed Fund for Science Research Graduate Fellowship, and the Research Excellence Doctoral Fellowship at Syracuse University. S.D. also thanks the Kavli Institute for Theoretical Physics (KITP), where portions of this work were completed. KITP is supported in part by the National Science Foundation under grant No. NSF PHY-1748958. M.M. is grateful for support for this work provided by NASA through Einstein Postdoctoral Fellowship grant No. PF6-170169 awarded by the Chandra X-ray Center, which is operated by the Smithsonian Astrophysical Observatory for NASA under contract NAS8-03060. Support for program No. 14574 was provided by NASA through a grant from the Space Telescope Science Institute, which is operated by the Association of Universities for Research in Astronomy, Inc., under NASA contract NAS 5-26555. This material is based on work supported by the National Science Foundation under grant No. 1909203. E.R.-R. and R.W.E. thank the David and Lucile Packard Foundation, the Heising-Simons Foundation, and the Danish National Research Foundation (DNRF132) for support. R.W.E. is supported by the Eugene V. Cota-Robles Fellowship and National Science Foundation Graduate Research Fellowship Program (Award No. 1339067). A.A. is supported by the Berkeley Graduate Fellowship and the Cranor Fellowship. Resources supporting this work were provided by the NASA High-End Computing (HEC) Program through the NASA Advanced Supercomputing (NAS) Division at Ames Research Center, by the Institute for Advanced Study, by the University of Copenhagen high-performance computing cluster funded by a grant from VILLUM FONDEN (project No. 16599), and by Syracuse University. Any opinions, findings, and conclusions or recommendations expressed in this material are those of the authors and do not necessarily reflect the views of the National Science Foundation.

Software: FLASH (Fryxell et al. 2000), yt (Turk et al. 2011), Astropy (Astropy Collaboration 2013, 2018), Plotly (Plotly 2015), Matplotlib (Hunter 2007).

Appendix A
Fitting Formulae to Coefficients of Drag and Accretion

We present fitting formulae for the coefficients of accretion C_a and drag force C_d as a function of the mass ratio q_r and upstream Mach number $\mathcal{M}_\infty$ from both our $\gamma = 4/3$ and $\gamma = 5/3$ simulations. Fits are constructed using the q_r, $\mathcal{M}_\infty$, C_a, C_d data sets presented in Tables 1 and 2 in Section 3. The fits show a mapping from the simulation results to the input parameters for the parameter space we have explored. For the $\gamma = 4/3$ simulations, we use third-order polynomials as fitting functions for both $\log_{10}C_a$ and $\log_{10}C_d$, which are expressed as follows:

$$\log_{10} C_a = a_1 + a_2 q_r + a_3 \mathcal{M}_\infty + a_4 q_r \mathcal{M}_\infty + a_5 q_r^2 + a_6 \mathcal{M}_\infty^2 + a_7 q_r \mathcal{M}_\infty^2 + a_8 q_r^2 \mathcal{M}_\infty + a_9 q_r^3 + a_{10} \mathcal{M}_\infty^3 \quad \text{(A1)}$$

$$\log_{10} C_d = d_1 + d_2 q_r + d_3 \mathcal{M}_\infty + d_4 q_r \mathcal{M}_\infty + d_5 q_r^2 + d_6 \mathcal{M}_\infty^2 + d_7 q_r \mathcal{M}_\infty^2 + d_8 q_r^2 \mathcal{M}_\infty + d_9 q_r^3 + d_{10} \mathcal{M}_\infty^3. \quad \text{(A2)}$$

Accumulation of material from accretion onto an embedded compact object requires either that the object be a black hole or the presence of an effective cooling channel if the object has a surface. In the case of objects with a surface, accretion releases gravitational potential energy and generates feedback. Our simulations include a completely absorbing central boundary condition, and therefore our setup is appropriate for calculating accretion rates for cases where the feedback from accretion can be neglected. The fitting formulae from the $\gamma = 4/3$ simulations presented above are applicable for systems where a black hole is inspiraling inside the envelope of a more massive giant branch star. This is because, taking into account the minimum mass of black holes and the fact that the envelope must belong to a more massive giant star than the embedded object, the mass of the giant star in this scenario would be greater than $\sim 10 M_\odot$. As mentioned earlier, the flow of material in such high-mass stars would be represented by a $\gamma = 4/3$ equation of state.

For the $\gamma = 5/3$ simulations, we use second-order polynomials as fitting functions for both $\log_{10}C_a$ and $\log_{10}C_d$, which can be expressed as

$$\log_{10} C_a = a_1 + a_2 q_r + a_3 \mathcal{M}_\infty + a_4 q_r \mathcal{M}_\infty + a_5 q_r^2 + a_6 \mathcal{M}_\infty^2 \quad \text{(A3)}$$

Table A1
Coefficients of Fitting Formula for the Efficiency of Accretion and Drag from $\gamma = 4/3$ Simulations: Least-squares Solutions for the $\log_{10}C_a$ and $\log_{10}C_d$ Third-order Polynomial Fits

a_1	a_2	a_3	a_4	a_5	a_6	a_7	a_8	a_9	a_{10}
0.8169	−9.9784	0.1382	−0.4803	46.9755	−0.3330	0.6713	−4.1620	−58.9379	0.0379
d_1	d_2	d_3	d_4	d_5	d_6	d_7	d_8	d_9	d_{10}
0.5510	0.4502	−0.6741	0.5946	−14.9500	0.3159	−0.0203	−1.7043	30.4494	−0.0309

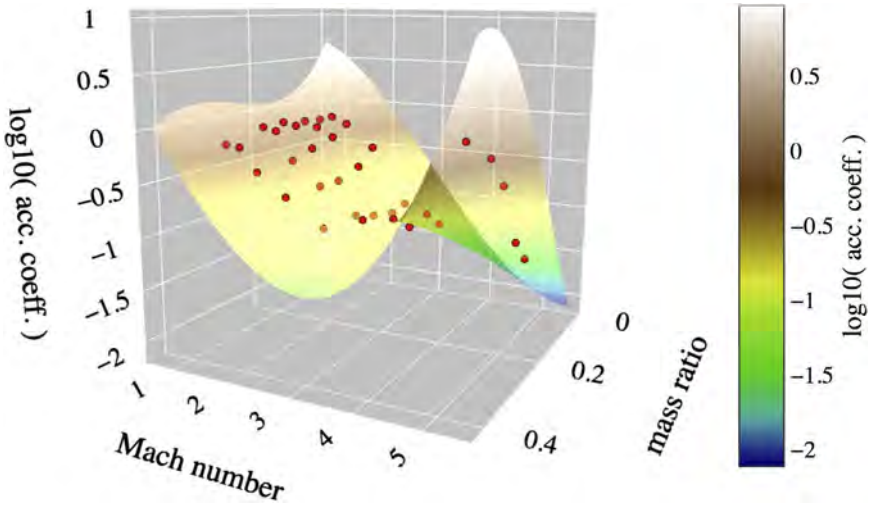

Figure A1. Relation between the coefficient of accretion, mass ratio, and upstream Mach number—$\log_{10} C_a(q_r, \mathcal{M}_\infty)$ for $(\Gamma, \gamma) = (4/3, 4/3)$ flows. The red circles represent the $\log_{10} C_a$ results obtained from the hydrodynamic simulations with q_r and $\mathcal{M}_\infty$ parameters. The three-dimensional surface shows the best-fitting third-order polynomial relation of $\log_{10} C_a$ in terms of $(q_r, \mathcal{M}_\infty)$. (An interactive version of this figure is available.)

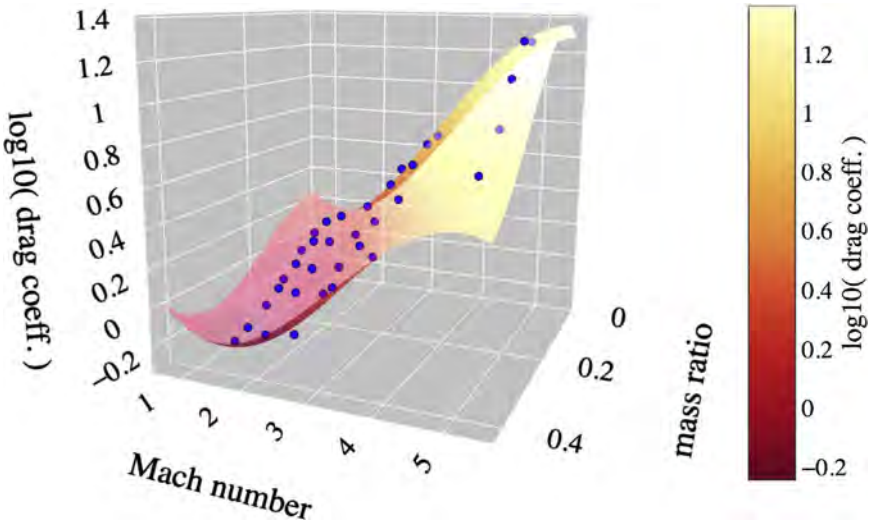

Figure A2. Relation between the coefficient of drag, mass ratio, and upstream Mach number—$\log_{10} C_d(q_r, \mathcal{M}_\infty)$ for $(\Gamma, \gamma) = (4/3, 4/3)$ flows. The blue circles represent the $\log_{10} C_d$ results obtained from the hydrodynamic simulations with q_r and $\mathcal{M}_\infty$ parameters. The three-dimensional surface shows the best-fitting third-order polynomial relation of $\log_{10} C_d$ in terms of $(q_r, \mathcal{M}_\infty)$. (An interactive version of this figure is available.)

Table A2
Coefficients of Fitting Formula for the Efficiency of Accretion and Drag from $\gamma = 5/3$ Simulations: Least-squares Solutions for the $\log_{10} C_a$ and $\log_{10} C_d$ Second-order Polynomial Fits

a_1	a_2	a_3	a_4	a_5	a_6
0.9184	−0.9619	−1.2057	1.2247	−2.480	0.1150233
d_1	d_2	d_3	d_4	d_5	d_6
−0.1552	−3.0323	0.2756	0.1976	1.4186	−0.0092

$$\log_{10} C_d = d_1 + d_2 q_r + d_3 \mathcal{M}_\infty + d_4 q_r \mathcal{M}_\infty + d_5 q_r^2 + d_6 \mathcal{M}_\infty^2. \quad \text{(A4)}$$

These fitting formulae from the $\gamma = 5/3$ simulations are applicable for systems where a white dwarf or a main-sequence star is inspiraling inside the envelope of a more massive giant branch star. The giant star in this case would be less massive than that in the $\gamma = 4/3$ systems. However, despite flow convergence in such systems, we do not expect significant mass accumulation from accretion onto the compact object owing to the lack of an apparent cooling mechanism. Main-sequence stars and white dwarfs are not compact enough to promote cooling channels such as neutrino

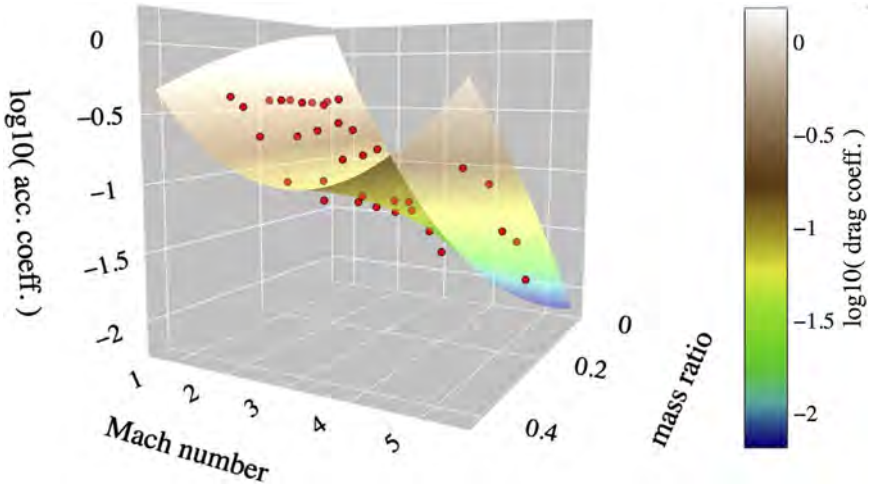

Figure A3. Relation between the coefficient of accretion, mass ratio, and upstream Mach number—$\log_{10} C_a(q_r, \mathcal{M})$ for $(\Gamma, \gamma) = (5/3, 5/3)$ flows. The red circles represent the $\log_{10} C_a$ results obtained from the hydrodynamic simulations with q_r and $\mathcal{M}_\infty$ parameters. The three-dimensional surface shows the best-fitting second-order polynomial relation of $\log_{10} C_a$ in terms of $(q_r, \mathcal{M}_\infty)$. (An interactive version of this figure is available.)

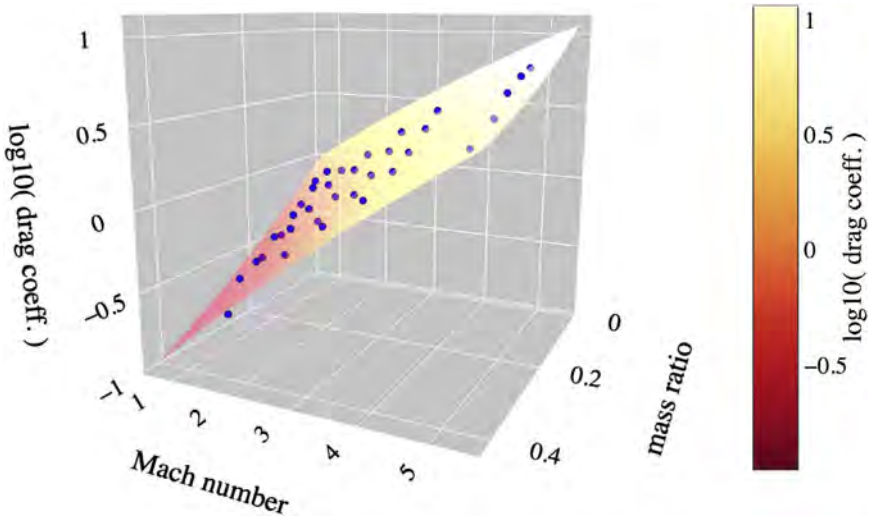

Figure A4. Relation between the coefficient of drag, mass ratio, and upstream Mach number—$\log_{10} C_d(q_r, \mathcal{M}_\infty)$ for $(\Gamma, \gamma) = (5/3, 5/3)$ flows. The blue circles represent the $\log_{10} C_d$ results obtained from the hydrodynamic simulations with q_r and $\mathcal{M}_\infty$ parameters. The three-dimensional surface shows the best-fitting second-order polynomial relation of $\log_{10} C_d$ in terms of $(q_r, \mathcal{M}_\infty)$. (An interactive version of this figure is available.)

emission, mediating the luminosity of the accretion onto the neutron stars. Also, the common envelope flows are optically thick, preventing the escape of heat through photon diffusion. It would be more appropriate to model these objects with a hard-surface boundary condition than an absorbing boundary condition.

The least-squares solutions we obtain for the fits to the $\gamma = 4/3$ and $\gamma = 5/3$ data sets are tabulated in Tables A1 and A2, respectively. In Figures A1–A4 we present the $\log_{10} C_a(q_r, \mathcal{M}_\infty)$ and $\log_{10} C_d(q_r, \mathcal{M}_\infty)$ data sets from the $\gamma = 4/3$ and $\gamma = 5/3$ simulations. Overlaid are the best-fit surfaces as presented in Equations (A1)–(A4) above. Interactive versions of these figures can be viewed at https://soumide1102.github.io/common-envelope-hydro-paper and in the online Journal article.

Appendix B
Comparison with Other Studies Measuring Drag Forces

Several studies have looked at the evolution of drag forces in common envelope interactions with numerical simulations and analytical modeling and have compared them to the linear estimates from the HL formalism. In our simulations, we have modeled the regime where the upstream Mach numbers are greater than 1. This limits the applicability of our results to the dynamical inspiral phase, during which the embedded object falls supersonically through the common envelope. The resulting gaseous dynamic friction forces have been modeled analytically in Ostriker (1999) and numerically, in the context of common envelope phases, in Staff et al. (2016), Reichardt et al. (2019), and Chamandy et al. (2019a), allowing comparison of their results with those from our work.

Ostriker (1999) used time-dependent linear perturbation theory to evaluate the dynamical friction force on a massive perturber in an infinite, homogeneous, gaseous medium, when moving both supersonically and subsonically. The Ostriker (1999) results define the strength of the dynamical friction relative to the size of the wake the object has created.

Among the global simulations of common envelope phases, Staff et al. (2016) modeled an extreme mass ratio system

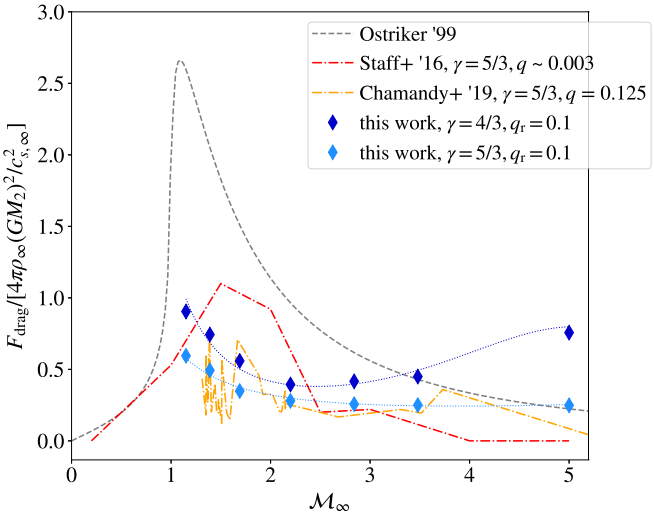

Figure B1. Comparison of the evolution of drag forces with upstream Mach number obtained from "wind tunnel" simulations in this work with other efforts to estimate drag forces applicable to common envelope interactions. Plotted are drag force estimates (i) on a massive perturber in a gaseous medium, derived analytically in Ostriker (1999); (ii) from global simulations in Staff et al. (2016) modeling a common envelope interaction with binary mass ratio $q \approx 0.003$ and gas adiabatic index $\gamma = 5/3$; (iii) from global simulations in Chamandy et al. (2019a) modeling a common envelope interaction with binary mass ratio $q \approx 0.125$ and gas adiabatic index $\gamma = 5/3$; and (iv) from local simulations in this work modeling the common envelope dynamical inspiral phase with binary mass ratio $q \approx 0.1$ and gas adiabatic indices $\gamma = 4/3$ and $\gamma = 5/3$.

($q \approx 0.003$), with gas adiabatic index $\gamma = 5/3$. In the supersonic regime, their numerical drag force is ≈2–3 times larger than the HL drag force, as described by Equation (4). Reichardt et al. (2019) modeled a moderate mass ratio regime, $q \approx 0.6$. The numerical drag forces obtained from their simulation were within a factor of ≈2 of the drag forces calculated using the analytical approximation from the HL formalism (Equation (4)), which is in agreement with Staff et al. (2016). Chamandy et al. (2019a) performed global simulations for three different mass ratio cases, $q = 1/2, 1/4, 1/8$, with a gas adiabatic constant $\gamma = 5/3$. At their smallest q value of $1/8$, they find that the Bondi–HL estimates provide a good approximation for the drag force in their simulation. The differences between the simulation results and the Bondi–HL estimates increase with increasing q values, with a factor of 10 difference at their largest q value of $1/2$.

In Figure B1, we show the evolution of the drag forces (normalized by $[4\pi\rho_\infty (GM_2)^2/c_{s,\infty}^2]$) as a function of Mach numbers. We compare results obtained using the analytical approach in Ostriker (1999) with results obtained using the numerical approaches in Staff et al. (2016), Chamandy et al. (2019a), and this work. For the "Ostriker '99" curve, we use Equations (14) and (15) of Ostriker (1999), with $\ln(c_s t/r_{min}) = 4$, to obtain $F_{drag}/[4\pi\rho_\infty (GM_2)^2/v_\infty^2](\mathcal{M}_\infty)$, and then we divide $F_{drag}/[4\pi\rho_\infty (GM_2)^2/v_\infty^2](\mathcal{M}_\infty)$ by $\mathcal{M}_\infty^2$ to obtain $F_{drag}/[4\pi\rho_\infty (GM_2)^2/c_{s,\infty}^2](\mathcal{M}_\infty)$. For the "Staff+ '16" curve, we use Figure 4 in Staff et al. (2016) to extract the $F_{drag}/[4\pi\rho_\infty (GM_2)^2/c_{s,\infty}^2] - \mathcal{M}_\infty$ data. We divide the numerical drag force time series obtained from their high-resolution red giant branch simulations by the analytical drag force (including pressure effects) time series, to extract $F_{drag}/[4\pi\rho_\infty (GM_2)^2/v_\infty^2](t)$. We then divide $F_{drag}/[4\pi\rho_\infty (GM_2)^2/v_\infty^2](t)$ by the square of their Mach number time series data to obtain $F_{drag}/[4\pi\rho_\infty (GM_2)^2/c_{s,\infty}^2](t)$ and plot $F_{drag}/[4\pi\rho_\infty (GM_2)^2/c_{s,\infty}^2]$ ($\mathcal{M}_\infty$). For the "Chamandy+ '19" curve, we use the $q = 1/8$ panels from Figures 4 and 5 in Chamandy et al. (2019a) to extract the $F_{drag}/[4\pi\rho_\infty (GM_2)^2/c_{s,\infty}^2] - \mathcal{M}_\infty$ data. We divide their $R_a(t)$ by $H_\rho(t)$ data to get $\epsilon_\rho(t)$, and we use Equation (11) to get $\mathcal{M}_\infty(t)$ from $(\epsilon_\rho(t), q)$. We divide their numerical drag force time series by their analytical drag force time series (based on the Bondi–HL theory) to obtain $F_{drag}/[4\pi\rho_\infty (GM_2)^2/v_\infty^2](t)$, further divide $F_{drag}/[4\pi\rho_\infty (GM_2)^2/v_\infty^2](t)$ by $\mathcal{M}_\infty(t)^2$ to obtain $F_{drag}/[4\pi\rho_\infty (GM_2)^2/c_{s,\infty}^2](t)$, and plot $F_{drag}/[4\pi\rho_\infty (GM_2)^2/c_{s,\infty}^2]$ ($\mathcal{M}_\infty$). For closest comparisons with this work, we use our $q_r = 0.1$ simulation data and plot both $\gamma = 4/3$ and $5/3$ cases. We obtain $F_{drag}/[4\pi\rho_\infty (GM_2)^2/c_{s,\infty}^2](\mathcal{M}_\infty)$ on dividing $C_d(\mathcal{M}_\infty)$ by $\mathcal{M}_\infty^2$.

The overall pattern of evolution of the normalized drag is similar in all of these works. The magnitude of our drag force agrees with the corresponding values in the supersonic regime in the global simulations, to within a factor of 2. A combination of the data from all these works enables the understanding of the overall evolution of the drag force. As the object spirals in through the dynamical inspiral phase, it sweeps through the surrounding envelope supersonically. In this regime, the Mach number decreases as the object spirals deeper within the envelope. When the Mach number decreases below 1.0, a qualitative change occurs, and the coefficient of drag becomes significantly less than unity (e.g., Shima et al. 1985; Ostriker 1999). This causes a turnover in the drag force, and it decreases as the Mach number decreases through values less than 1.0. The decrease in drag force slows down the inspiral at late times of the spiral-in phase. In short, in the supersonic regime, HL theory provides an underestimate of drag forces, while in the subsonic regime, it dramatically overestimates the magnitude of the force.

Finally, we discuss the impact of different gas equations of state in simulations. As discussed in Section 3.5.3, the overall patterns of the evolution of drag forces with $\mathcal{M}_\infty$ and q_r are similar between our $\gamma = 4/3$ and $\gamma = 5/3$ simulations. However, the magnitude of drag coefficients in the $\gamma = 5/3$ case is lower than in the $\gamma = 4/3$ case. This suggests that the $\gamma = 5/3$ case would generate a slower orbital decay owing to lower drag forces. Studies such as Reichardt et al. (2020) have performed simulations with an ideal gas equation of state, as well as a tabulated equation of state with a range of effective γ as a function of density and temperature. The overall inspiral morphologies in their results are similar between the two models. The differences can be attributable to differences in the magnitudes of the coefficients of drag, which can generate a faster or slower orbital decay, depending on the equation of state.

ORCID iDs

Soumi De https://orcid.org/0000-0002-3316-5149
Morgan MacLeod https://orcid.org/0000-0002-1417-8024
Rosa Wallace Everson https://orcid.org/0000-0001-5256-3620
Andrea Antoni https://orcid.org/0000-0003-3062-4773
Ilya Mandel https://orcid.org/0000-0002-6134-8946
Enrico Ramirez-Ruiz https://orcid.org/0000-0003-2558-3102

References

Aasi, J., Abbott, B. P., Abbott, R., et al. 2015, CQGra, 32, 074001
Abbott, B. P., Abbott, R., Abbott, T. D., et al. 2016a, PhRvL, 116, 061102
Abbott, B. P., Abbott, R., Abbott, T. D., et al. 2016b, PhRvX, 6, 041015
Abbott, B. P., Abbott, R., Abbott, T. D., et al. 2017a, PhRvL, 118, 221101
Abbott, B. P., Abbott, R., Abbott, T. D., et al. 2017b, ApJL, 851, L35

Abbott, B. P., Abbott, R., Abbott, T. D., et al. 2017c, PhRvL, 119, 141101
Abbott, B. P., Abbott, R., Abbott, T. D., et al. 2019, PhRvX, 9, 031040
Acernese, F., Agathos, M., Agatsuma, K., et al. 2015, CQGra, 32, 024001
Antoni, A., MacLeod, M., & Ramirez-Ruiz, E. 2019, ApJ, 884, 22
Astropy Collaboration 2013, A&A, 558, A33
Astropy Collaboration 2018, AJ, 156, 123
Bailyn, C. D., Jain, R. K., Coppi, P., & Orosz, J. A. 1998, ApJ, 499, 367
Batta, A., & Ramirez-Ruiz, E. 2019, arXiv:1904.04835
Bavera, S. S., Fragos, T., Qin, Y., et al. 2020, A&A, 635, 97
Belczynski, K., Buonanno, A., Cantiello, M., et al. 2014, ApJ, 789, 120
Belczynski, K., Holz, D. E., Bulik, T., & O'Shaughnessy, R. 2016, Natur, 534, 512
Bethe, H. A., & Brown, G. E. 1998, ApJ, 506, 780
Biwer, C. M., Capano, C. D., De, S., et al. 2019, PASP, 131, 024503
Blondin, J. M., & Raymer, E. 2012, ApJ, 752, 30
Bondi, H., & Hoyle, F. 1944, MNRAS, 104, 273
Brown, G. E. 1995, ApJ, 440, 270
Chamandy, L., Blackman, E. G., Frank, A., et al. 2019a, MNRAS, 490, 3727
Chamandy, L., Frank, A., Blackman, E. G., et al. 2018, MNRAS, 480, 1898
Chamandy, L., Tu, Y., Blackman, E. G., et al. 2019b, MNRAS, 486, 1070
Chandrasekhar, S. 1943, ApJ, 97, 255
Chevalier, R. A. 1993, ApJL, 411, L33
de Marco, O., & Izzard, R. G. 2017, PASA, 34, e001
De, S., Biwer, C. M., Capano, C. D., Nitz, A. H., & Brown, D. A. 2019, Scientific Data, 6, 81
Edgar, R. 2004, NewAR, 48, 843
Eldridge, J. J., & Stanway, E. R. 2016, MNRAS, 462, 3302
Everson, R. W., MacLeod, M., De, S., Macias, P., & Ramirez-Ruiz, E. 2020, arXiv:2006.07471
Farr, B., Holz, D. E., & Farr, W. M. 2018, ApJL, 854, L9
Farr, W. M., Sravan, N., Cantrell, A., et al. 2011, ApJ, 741, 103
Farr, W. M., Stevenson, S., Coleman Miller, M., et al. 2017, Natur, 548, 426
Fragos, T., Andrews, J. J., Ramirez-Ruiz, E., et al. 2019, ApJL, 883, L45
Fryxell, B., Olson, K., Ricker, P., et al. 2000, ApJS, 131, 273
Fryxell, B., & Taam, R. 1989, ApJ, 335, 862
Fryxell, B., Taam, R., & McMillan, S. 1987, ApJ, 315, 536
Fuller, J., & Ma, L. 2019, ApJL, 881, L1
Han, Z., Podsiadlowski, P., & Eggleton, P. P. 1994, MNRAS, 270, 121
Han, Z., Podsiadlowski, P., Maxted, P. F. L., Marsh, T. R., & Ivanova, N. 2002, MNRAS, 336, 449
Hoyle, F., & Lyttleton, R. A. 1939, PCPS, 35, 405
Hunter, J. D. 2007, CSE, 9, 90
Iaconi, R., de Marco, O., Passy, J.-C., & Staff, J. 2018, MNRAS, 477, 2349
Iaconi, R., Reichardt, T., Staff, J., et al. 2017, MNRAS, 464, 4028
Iben, I. J., & Livio, M. 1993, PASP, 105, 1373
Ivanova, N., Justham, S., Chen, X., et al. 2013, A&ARv, 21, 59
Ivanova, N., & Nandez, J. L. A. 2016, MNRAS, 462, 362
King, A. R., & Kolb, U. 1999, MNRAS, 305, 654
Kreidberg, L., Bailyn, C. D., Farr, W. M., & Kalogera, V. 2012, ApJ, 757, 36
Kruckow, M. U., Tauris, T. M., Langer, N., et al. 2016, A&A, 596, A58
Kushnir, D., Zaldarriaga, M., Kollmeier, J. A., & Waldman, R. 2016, MNRAS, 462, 844
Lucy, L. B. 1967, AJ, 72, 813
MacLeod, M., Antoni, A., Murguia-Berthier, A., Macias, P., & Ramirez-Ruiz, E. 2017, ApJ, 838, 56
MacLeod, M., & Ramirez-Ruiz, E. 2015a, ApJ, 803, 41
MacLeod, M., & Ramirez-Ruiz, E. 2015b, ApJL, 798, L19
Mandel, I., & Farmer, A. 2018, arXiv:1806.05820
Mapelli, M. 2018, arXiv:1809.09130
Marchant, P., Langer, N., Podsiadlowski, P., Tauris, T. M., & Moriya, T. J. 2016, A&A, 588, A50
Murguia-Berthier, A., MacLeod, M., Ramirez-Ruiz, E., Antoni, A., & Macias, P. 2017, ApJ, 845, 173
Nandez, J. L. A., Ivanova, N., & Lombardi, J. C. J. 2015, MNRAS: Letters, 450, L39
Nitz, A. H., Capano, C., Nielsen, A. B., et al. 2019, ApJ, 872, 195
Nitz, A. H., Dent, T., Davies, G., et al. 2020, ApJ, 891, 123
Ohlmann, S. T., Röpke, F. K., Pakmor, R., & Springel, V. 2016a, ApJL, 816, L9
Ohlmann, S. T., Röpke, F. K., Pakmor, R., Springel, V., & Müller, E. 2016b, MNRAS, 462, L121
Ostriker, E. C. 1999, ApJ, 513, 252
Özel, F., Psaltis, D., Narayan, R., & McClintock, J. E. 2010, ApJ, 725, 1918
Paczynski, B. 1976, in IAU Symp. 73, Structure and Evolution of Close Binary Systems, ed. P. Eggleton, S. Mitton, & J. Whelan (Cambridge: Cambridge Univ. Press), 75
Passy, J.-C., Marco, O. D., Fryer, C. L., et al. 2012, ApJ, 744, 52
Piran, Z., & Piran, T. 2020, ApJ, 892, 64
Plotly 2015, Collaborative Data Science (Montreal, QC: Plotly Technologies Inc.), https://plot.ly
Reichardt, T., de Marco, O., Iaconi, R., Tout, C. A., & Price, D. J. 2019, MNRAS, 484, 631
Reichardt, T., de Marco, O., Iaconi, R., Chamandy, L., & Price, D. J. 2020, MNRAS, 494, 5333
Ricker, P. M., & Taam, R. E. 2007, ApJL, 672, L41
Ricker, P. M., & Taam, R. E. 2012, ApJ, 746, 74
Roxburgh, I. W. 1967, Natur, 215, 838
Ruffert, M. 1994, A&AS, 106, 505
Ruffert, M. 1995, A&AS, 113, 133
Ruffert, M., & Arnett, D. 1994, ApJ, 427, 351
Sandquist, E., Taam, R. E., Lin, D. N. C., & Burkert, A. 1998, ApJL, 506, L65
Schrøder, S. L., Batta, A., & Ramirez-Ruiz, E. 2018, ApJL, 862, L3
Shima, E., Matsuda, T., Takeda, H., et al. 1985, MNRAS, 217, 367
Smarr, L. L., & Blandford, R. 1976, ApJ, 207, 574
Staff, J., de Marco, O., Wood, P., et al. 2016, MNRAS, 458, 832
Stevenson, S., Vigna-Gómez, A., Mandel, I., et al. 2017, NatCo, 8, 14906
Taam, R., & Fryxell, B. 1989, ApJ, 339, 297
Taam, R. E., Bodenheimer, P., & Ostriker, J. P. 1978, ApJ, 222, 269
Taam, R. E., & Ricker, P. M. 2010, NewAR, 54, 65
Tiwari, V., Fairhurst, S., & Hannam, M. 2018, ApJ, 868, 140
Turk, M. J., Smith, B. D., Oishi, J. S., et al. 2011, ApJS, 192, 9
van den Heuvel, E. P. J. 1976, in IAU Symp. 73, Structure and Evolution of Close Binary Systems, ed. P. Eggleton, S. Mitton, & J. Whelan (Cambridge: Cambridge Univ. Press), 35
Venumadhav, T., Zackay, B., Roulet, J., Dai, L., & Zaldarriaga, M. 2020, PhRvD, 101, 083030
Woosley, S. E. 2017, ApJ, 836, 244
Yusof, N., Hirschi, R., Meynet, G., et al. 2013, MNRAS, 433, 1114
Zackay, B., Venumadhav, T., Dai, L., Roulet, J., & Zaldarriaga, M. 2019, PhRvD, 100, 023007
Zaldarriaga, M., Kushnir, D., & Kollmeier, J. A. 2018, MNRAS, 473, 4174